Heterostructure-based devices with enhanced humidity stability for H$_2$ gas sensing applications in breath tests and portable batteries

Oleg Lupan [a,b,*], Nicolai Ababii [b], Abhishek Kumar Mishra [c,**], Mani Teja Bodduluri [d], Nicolae Magariu [b], Alexander Vahl [e], Helge Krüger [a], Bernhard Wagner [d], Franz Faupel [e], Rainer Adelung [a,**], Nora H. de Leeuw [f,g,**], Sandra Hansen [a,**]

[a] Institute for Materials Science, Chair for Functional Nanomaterials, Faculty of Engineering, Kiel, Kaiserstraße 2, D-24143, Kiel, Germany
[b] Center for Nanotechnology and Nanosensors, Department of Microelectronics and Biomedical Engineering, Faculty CIM, Technical University of Moldova, 168 Stefan cel Mare str., MD-2004, Chisinau, Republic of Moldova
[c] School of Engineering, Department of Physics, University of Petroleum and Energy Studies, Bidholi via Premnagar, Dehradun, 248007, India
[d] Institute for Materials Science, Chair for Materials and Processes for Nanosystem Technologies, Christian-Albrechts-University of Kiel, Kaiser str. 2, D 24143, Kiel, Germany
[e] Institute for Materials Science, Chair for Multicomponent Materials, Faculty of Engineering, Kiel, Kaiserstraße 2, D-24143, Kiel, Germany
[f] School of Chemistry, University of Leeds, Leeds, LS2 9JT, United Kingdom
[g] School of Earth Sciences, Utrecht University, Princetonlaan 8a, 3584 CB, Utrecht, the Netherlands

ARTICLE INFO

ABSTRACT

Semiconducting metal oxide - based gas sensors exhibit outstanding sensitivity, although humidity in the analyte typically hampers precise measurements. In this work it was shown that a 5−6 nm thin Al$_2$O$_3$ nano-layer is particularly beneficial in reducing the interference due to humidity of p-type conductivity copper oxide-based gas sensors. An effective approach from chemical solutions at 75 °C and thermal annealing at 600 °C was used to grow copper oxide nano-crystallite layers. The Al$_2$O$_3$ nano-layers were subsequently deposited on top of copper oxide by atomic layer deposition in a high-aspect-ratio regime at 75 °C. The morphological, structural, chemical, vibrational, electronic and sensor characteristics of the heterostructured nano-crystallite layers have been studied. The final nano-Al$_2$O$_3$/CuO heterostructure showed an increase in the response to H$_2$ gas by 140 %, while long-term stability at low and high relative humidity was observed. The initial sensing response varied by only 10 % for an Al$_2$O$_3$ layer of 5−6 nm on top of CuO with a post-thermal annealing at 600 °C acting as an effective barrier for water vapor and oxygen. A comparison with CuO nanocrystallite layers covered by ALD with 6 nm and 15 nm of Al$_2$O$_3$ ultra-thin films on top demonstrates an exceptional stability of the hydrogen gas response at high relative humidity (84 % RH). Density functional theory-based calculations showed that the H$_2$ molecule spontaneously dissociates over the formed Al$_2$O$_3$/CuO heterostructure, interacting strongly with the surface Al atoms, showing different behavior compared to the pristine CuO (111) surface, where H$_2$ gas molecules are known to form water over the surface. The present study demonstrates that a thorough optimization of technology and surface properties due to coverage and formation of heterostructured nano-materials improves the humidity stability during H$_2$ gas sensing applications which is important for real-world applications, e.g. portable battery analysis, H$_2$ breath tests, along with environmental, medicine, security, and food safety diagnostic tests.

© 2021 Elsevier B.V. All rights reserved.

1. Introduction

A variety of semiconductor metal oxides (SMO) of different compositions are fabricated as nano-crystallite thin films for either gas sensing devices or as active layers for chemi-resistor based sensing applications. A significant amount of data has been published on the characteristics, structure and performance of sensor structures composed of different SMO materials [1–4]. However, the sensitiv-

* Corresponding author at: Institute for Materials Science, Chair for Functional Nanomaterials, Faculty of Engineering, Kiel, Kaiserstraße 2, D-24143, Kiel, Germany, Center for Nanotechnology and Nanosensors, Technical University of Moldova, 168 Stefan cel Mare str., MD-2004, Chisinau, Republic of Moldova.
** Corresponding authors.
E-mail addresses: ollu@tf.uni-kiel.de, oleg.lupan@mib.utm.md (O. Lupan), akmishra@ddn.upes.ac.in (A.K. Mishra), ra@tf.uni-kiel.de (R. Adelung), n.h.deleeuw@leeds.ac.uk (N.H. de Leeuw), sn@tf.uni-kiel.de (S. Hansen).

ity of almost all conductometric sensors to water vapor [5,6] is one of the major challenges for their practical application. The water in the analyte or tested ambience leads to a decrease or disappearance of the response, as well as fatal errors in the SMO sensors [7].

To reduce the effect of humidity and water in the analyte or tested ambience on the sensor performance, additional, code-posited materials on the sensor surface can be employed, e.g. ultra-thin films, organometallic films [8], metal-organic compounds based on zeolitic imidazolate frameworks [9], or tin dioxide powder by spark discharge [10]. Konvalina and Haick have reported the influence of the relative humidity on micro- and nano-particle-based chemical sensors for real-world purposes and the importance of humidity compensation [11]. Garg et al. have reported that the long-term drift of chemi-resistor characteristics based on Au metal mono-layer-capped nano-particles (NPs) can be decreased by capping them with tri-thiols rather than mono-thiols, thus slowing down the oxidation process of the surface thiolates [12]. Javey *et al.* have reported an approach to eliminate effects of response/sensitivity to relative humidity (RH) for chemical-sensitive field-effect transistors (FET) by employing micro-heaters [13].

The continuous monitoring of various biological and gaseous species that contain humidity in their surroundings is of high importance due to hazardous emissions, breath tests, and environmental pollution, but implementation remains challenging. For example, hydrogen gas breath tests are developed to investigate pathophysiology of gastrointestinal diseases or intestinal disorders [14]. It is well known that intestinal bacteria in the bowel yield H_2 gas on fermentation of carbohydrates, most commonly lactulose, in patients with suspicious small intestinal bacterial overgrowth [15,16]. Bacteria in the bowel can do so only if dietary carbo-hydrates are not absorbed in the small intestine and remain as undigested material as they transit along the digestive tract to the large intestine. Thus, glucose H_2 gas breath tests that are immune to relative humidity (RH) from the exhaled atmosphere can help significantly to overcome current challenges in diagnosis and to develop new portable devices for biomedical applications, since existing breath test structures pose several challenges because of RH on the signal. Appropriate and convenient appraisals of diagnostic tests can reduce healthcare costs and increase the specificity of care to patient [17]. The quality of the real information received from diagnostic tests can be enhanced if the methodology and approach of the test development meets all standards related to quality [17]. In this context, the most important qualities of semi-conductor metal oxide-based hydrogen gas sensors are the gas sensitivity, gas response, response and recovery times, operating temperature, temperature stability, and especially the selectivity. All these characteristics are extensively investigated and improved in the development of new materials [18–21]. For example, it is known that adsorption of H_2O molecules on oxide surfaces of SMOs will decrease the H_2 gas response [19,20,22–24]. In our previous work [5], the effect of relative humidity on the response of nanostructured films on Zn-doped copper oxide was demonstrated. Moreover, Hübner et al. [6] demonstrated the effect of humidity on CO detection based on thick CuO films. However, further investigation is essential to increase the stability and to reduce the interference of relative humidity and enhance reliable long-term operation, since RH significantly affects sensor performances. For example, it is important to note, that relative humidity is the main cause of the lack in performance of SMO sensors. Even at very low values of RH, most SMO sensors are strongly affected, as reported by Wicker et al., where the sensor resistance was already affected at low RH of 0.1 % [25], and with increasing RH, the sensor response is affected even more [25,26]. Thus, many efforts are made world-wide to reduce the influence of RH in the test environment as a

major factor to improve the quality of hydrogen sensing in breath tests, especially by semiconductor oxide-based sensors [19,20].

The surface reaction among the adsorbed oxygen species and the H_2O will reduce the baseline electrical resistance of the sensing material, thus lowering the gas response value [19,20]. Additionally, H_2O molecules adsorbed on the semiconducting oxide surface will block active surface sites, thereby lowering the gas response even further. In addition to these considerations, the RH influences the sensing performance of oxide materials in terms of sensor stability and reliability [27], since it affects repeatability of the sensing performance.

Another important aspect to consider are the "necks" between crystal grains, their sizes, and boundaries along with surface defects that can change during long-term operation at high temperatures, leading to a variation of H_2 responses under the same conditions and decreased sensor stability [19,28]. Therefore, the protection of the sensing film with an additional thin oxide layer using high aspect ratio deposition for example by atomic layer deposition (ALD) of another oxide as ultra-thin layer on top, would contribute to solving this issue. In ALD, alternating pulses of chemical precursor vapors are injected onto the sample surface to form a single atomic layer each cycle. Furthermore, this method allows the accurate control of the film thickness at the nanometer scale. Consequently, a pinhole-free and uniform film is grown, which acts as a barrier to water vapor and oxygen. Moreover, the long-term stability, which is a key factor for gas sensors from polycrystalline materials, can be improved as well. Thus, the influence of humidity on the H_2 gas response should be eliminated, either through the design of the materials (surface structure and facet control) [29], by exploring different device structures, or by inducing humidity compensation to the response/sensitivity in the driving circuit, which otherwise deteriorate the practical applications of the oxide-based sensors.

In this work CuO nanocrystallite layers covered with a 6 nm and 15 nm Al_2O_3 ALD ultra-thin films are presented with exceptional stability and a hydrogen gas response at high relative humidity (84 % RH). Heterostructure oxide-based H_2 gas sensors that show extraordinary selectivity over other gaseous molecules and stability in the presence of humidity are reported. The sensing characteristics of such heterostructures are drastically improved by the heterojunction formed with the top Al_2O_3 layer on CuO polycrystalline films. This enhancement is linked to the exploitation of the electronic sensitization and surface structuring, which will be discussed in detail.

2. Experimental methods

2.1. Sample synthesis

Sample synthesis from chemical solutions (SCS) followed by thermal treatment/annealing (TA) were used to prepare copper oxide nanocrystalline layers on a glass substrate [30]. The copper-complex aqueous solution, as cation bath, was made by a 0.9 M $CuSO_4 \cdot 6H_2O$ and 0.9 M $Na_2S_2O_3 \cdot 6H_2O$. Deposition cycles of copper oxide film consist of consecutive steps: (a) substrate holding in the alkali bath (81 °C) for the adsorption of the ions OH– on the microscope specimen; (b) substrate holding in the $Na_2S_2O_3 \cdot 5H_2O$ for reaction of the Cu^+ with adsorbed OH–.

$$2Cu^+ + 2OH^- \rightarrow 2CuOH \rightarrow Cu_2O + H_2O \tag{1}$$
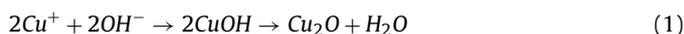
Conventional thermal treatment in a furnace at 600 °C for 30 min was used for post-deposition thermal annealing (TA), which approach significantly improves the crystallinity of the SCS grown copper oxide layers.

Al_2O_3 ultra-thin film growth via thermal ALD was realized using Picosun's R200 with the deposition temperature during the process adjusted to 75 °C. Additionally, Picoflow™ technology was utilized to achieve conform and uniform nano-layers with high aspect ratio (HAR). Trimethylaluminum (TMA) was used as the aluminum source and H_2O to oxidize chemisorbed TMA. Alternating pulses of the precursors were pulsed into the reactor chamber for 0.1 s per pulse to grow monolayers of Al_2O_3. Nitrogen gas was used to transport the precursor vapors into the reaction chamber and to purge byproducts from the reactor.

2.2. Sample characterization

The morphology of the hetero-structured specimens was investigated by Carl Zeiss SEM (6 kV, 8 μA). The analysis of composition was performed by EDX, in connection with Carl Zeiss SEM. Crystallographic spectra were measured with diffractometer X-ray (XRD) using a unit Seifert3000TT, at 35 mA and 40 kV, with $CuK_{\alpha}1$ irradiation (λ = 1.540598 Å). A microRaman study was executed using a WITec Raman spectrometer, with a 532 nm Nd-YAG laser, a Peltier-cooled detector.

Additional data on the stoichiometry and chemical composition of the (6 nm Al_2O_3)/CuO hetero-structures were measured by XPS (OmicronNanoTechnology with Al-anode, 240 W). After collecting the spectra, potential charging of the sample was corrected by setting the C1s line of aliphatic carbon to the reference value of 284.5 eV [31]. For the evaluation, the software CasaXPS (version 2.3.16) was employed. The sensing performances to test gas were using a heterostructure detector connected to gold electrodes (see Fig. 1(e–g)). The measuring apparatus is linked to a set-up with gas flow as described in previous works [20,27,32]. The responses (R) to gases were defined according to the expression $((R_{gas} − R_{air})/R_{air})·100$, having R_{air} and R_{gas} as the electrical resistances of the heterostructure when placed under atmosphere (R_{air}) and exposed to test gas or vapors (R_{gas}), respectively. While varying the operating temperature (OPT), volatile organic compounds (VOCs) and hydrogen were used as test gas or vapors with a flow of 500 sccm (ml/min) set using pre-calibrated mass flow controllers [32] and the required concentrations were obtained using the following equations to obtain the sensor performances of the specimen [33,34]:

$$C \ (ppm) = \frac{C_1 \cdot F_{gas}}{F_{tot}} \tag{2}$$

where C is the required concentration of gas; C_1 is the initial concentration of the test gas; F_{gas} is the gas flow; and F_{tot} is the total flow of the gas-air mixture.

$$V_x = (Vol \cdot C \cdot M)/(22.4 \cdot d \cdot p) \cdot \left[(273 + T_r)/(273 + T_c) \right] \cdot 10^{-9} \tag{3}$$

where V_x is the volume of VOC injected; Vol is the test chamber volume; C is the required VOC concentration (ppm); M is the molar mass; d the density (g/cm^3); p the purity; T_r the room temperature; and T_c is the test chamber temperature (operating temperature).

By measuring continuously, the output voltage across the heterostructure-based specimen, using a source meter (Keithley 2400) connected to a PC with suitable LabView (National Instruments) interface, the electrical conductivity was recorded under ambient atmosphere and exposed to test gas or vapors (VOCs and hydrogen). During the measurements the relative humidity was set using a bubbling system and was measured using a standard hygrometer [35].

2.3. Calculation details

Electronic structure calculations were carried out within a plane wave pseudopotential implementation of the density functional theory (DFT), using the projector augmented wave (PAW) method [36,37] within the Vienna ab-initio simulation package (VASP) [38–41]. Exchange correlations were treated by the generalized gradient approximation (GGA) using PBE functionals [42]. The Hubbard model was applied to improve the localisation of the Cu 3d electrons, through the formulation of Dudarev et al. [43], where an effective U parameter correction of U_{eff} = 7 eV (U_{eff} = U - J, i.e. the difference between the Coulomb U and exchange J parameters) was used to accurately describe the strong correlations in CuO. This value of the U parameter effectively reproduces the correct structural, magnetic and electronic properties of tenorite (CuO crystal) [44,45]. Other details of the calculations are the same as in previous work [44].

The (111) surface is the most stable surface of tenorite and was modelled using 3 × 3×1 Monkhorst − Pack grid points (atomic structures were relaxed using the tetrahedron method) [46]. The locations of the atoms in the cell were fully relaxed until the atomic forces on each ion were less than 0.01 eV/ Å. The electronic densities of states were computed using a dense 5 × 5 × 1 MonkhorstPack grid point matrix, whereas a truncation kinetic energy of 450 eV for the plane waves provides an accurate description of properties that are affected by sharp features in the density of states. We used our previous slab model of four atomic layers, where the bottom two layers of atoms were fixed at their relaxed bulk positions to simulate the bulk phase of the crystal, while the atoms in the top two layers of the surface were permitted to change their atomic coordinates freely during geometry optimization [44]. A vacuum region of more than 15 Å was used between surface slabs to avoid interactions between the periodic images while modelling the molecule-surface interactions.

For the investigations of the interactions of the gas molecules with the surface, we have incorporated long-range dispersion forces using the DFT-D2 approach by Grimme [47]. The adsorption energies of the gas molecule were calculated using the relation:

$$E_{ads} = E_{complex} − (E_{surface} + E_{molecule}) \tag{4}$$

where $E_{complex}$ is the total energy of the surface slab with adsorbed molecule, $E_{surface}$ is the energy of the surface slab without molecule, and $E_{molecule}$ is the energy of the isolated molecule. $E_{molecule}$ was calculated by modelling the isolated molecule in the centre of a broken symmetry cell with lattice constants of 20 Å, sampling only the gamma-point of the Brillouin zone with the same set of parameters as described for the surfaces. Bader charge analyses were performed using the code developed by Henkelman and co-workers [48,49] to investigate the charge transfer between the surface and molecule.

3. Results and discussions

3.1. Morphological investigations of Al_2O_3/CuO

Morphology and SEM images of (6 nm Al_2O_3)/CuO heterostructures with a 6 nm top layer of Al_2O_3 after thermal treatment at 600 °C for 30 min are shown in Fig. 1(a–d). The investigated samples are formed of densely packed CuO grains that homogenously cover the specimen. Agglomerates or gaps were not found, even at lower magnification (see Fig. S1). The diameter of the crystalline CuO grains fluctuates in a diapason from 100 nm to 450 nm (Fig. 1(b,c) and Fig. S2). At higher magnification (see Fig. 1(b,c) and Fig. S2(b,c)), a nanodot-like structure is observed for (6 nm Al_2O_3)/CuO heterostructures after TA at 600 °C for 30 min in comparison with as-grown samples with (6 nm Al_2O_3)/CuO (see Fig. S2(a)). These nanodot-like structures appear only for samples after thermal annealing at about 600 °C for 30 min, probably due to phase transitions at the interface or surface of the (6 nm Al_2O_3)/CuO. This
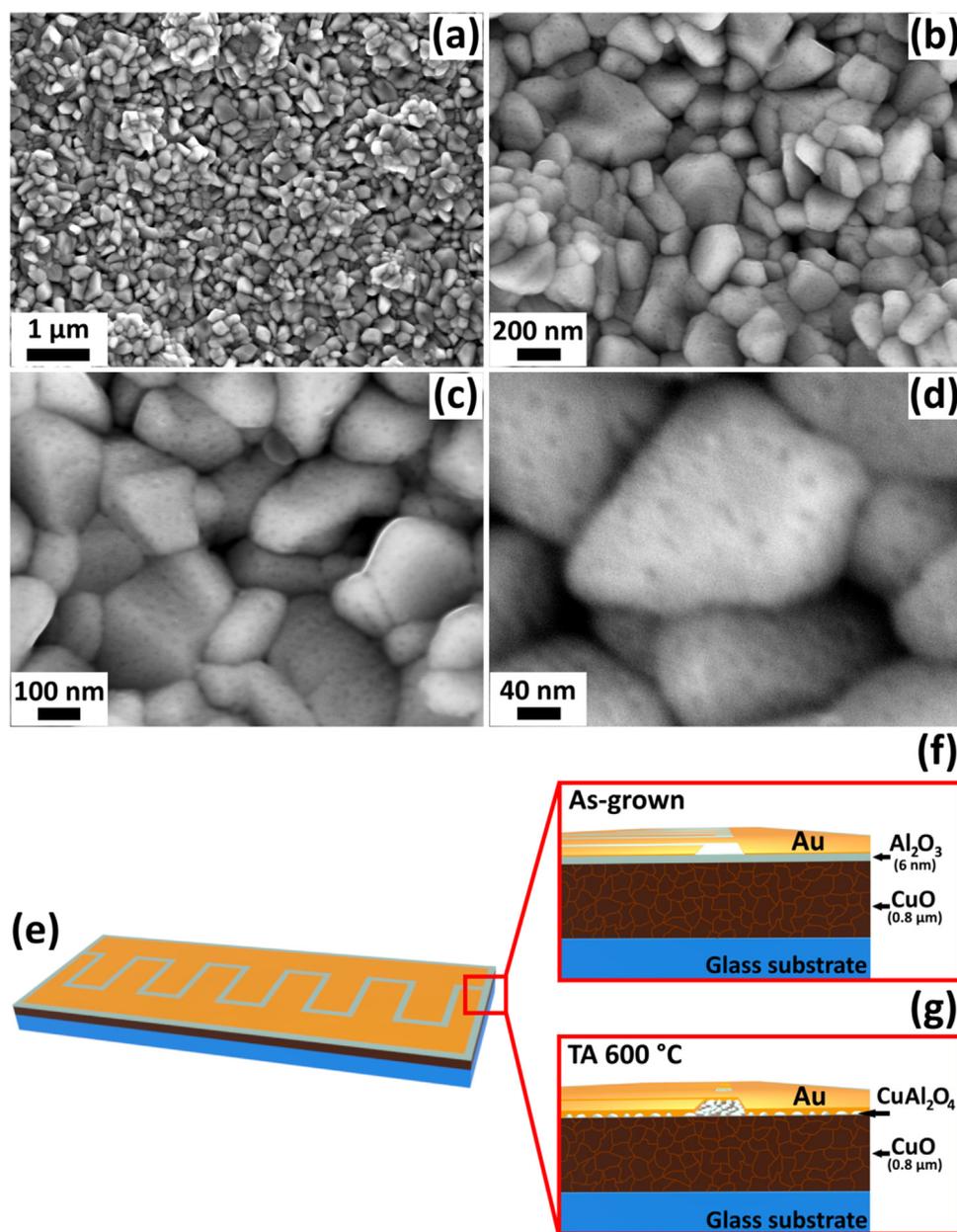
Fig. 1. SEM images of (6 nm Al_2O_3)/CuO heterostructures with thermal annealing at 600 °C for 30 min at various enlargement: (a) 1 μm; (b) 200 nm; (c) 100 nm; and (d) 40 nm. (e) The schematic drawing of the detector made on the nano-Al_2O_3/CuO heterostructure: (f) as-grown; and (g) TA at 600 °C.

process leads to the formation of nano-agglomerations of $CuAl_2O_4$ (see Fig. 1(**g**)), following the energy stress that occurs in this specific thermal annealing temperature range [50–52].

3.2. XRD, Raman and XPS studies

X-ray diffraction was selected to obtain the crystal structure of the Al_2O_3/CuO heterostructures after TA at 600 °C for 30 min. Fig. 2(**a**) shows that, for (6 nm Al_2O_3)/CuO heterostructures after TA at 600 °C for 30 min, the two phases of CuO and $CuAl_2O_4$ can be identified. As reported in our previous work [30], at temperatures above 550 °C, only monoclinic CuO is present with highest XRD reflections detected for (-111)/(002) and (111) at 2θ angles of 35.45° and 38.7°, respectively. The shape of the diffraction peaks indicates the high crystallinity of the investigated samples. The tenorite structure has space group C2/c [53] with crystal lattice parameters of c =5.1321 Å, a =4.6851 Å, b =3.4231 Å, and β = 99.52° [54]. The copper in tenorite

is in the Cu^{2+} oxidation state showing antiferromagnetic ordering [54] and antiferromagnetic insulating ground states [55,56]. For (15 nm Al_2O_3)/CuO heterostructures after TA at 620 °C for 40 min the two phases of CuO and $CuAl_2O_4$ were also identified (see **Fig. S3**).

The crystalline phase of $CuAl_2O_4$ was identified from Card PDF #01−1153 (copper aluminum oxide) to be a cubic system with the precise lattice parameter of a = 8.064 Å [50,57].

In Fig. 2(**b**), the Raman spectrum of (6 nm Al_2O_3)/CuO heterostructures at room temperature of 20 °C enclosed by 70 and 1000 cm^{-1} is shown. From the spectrum, the mode peaks observed at about (i) 281, 326 and 617 cm^{-1}, assigned to the tenorite [5,30], and (ii) 481, 512, 608, 703 and 788 cm^{-1}, which are assigned to the $CuAl_2O_4$ (copper aluminum oxide), confirm the existence of the two phases, also indicated by XRD [50]. Raman mapping image of the A_g mode (281 cm^{-1}) for the (6 nm Al_2O_3)/CuO heterostructures and TA at 600 °C in air for 30 min is shown in **Fig. S4**. The CuO structure
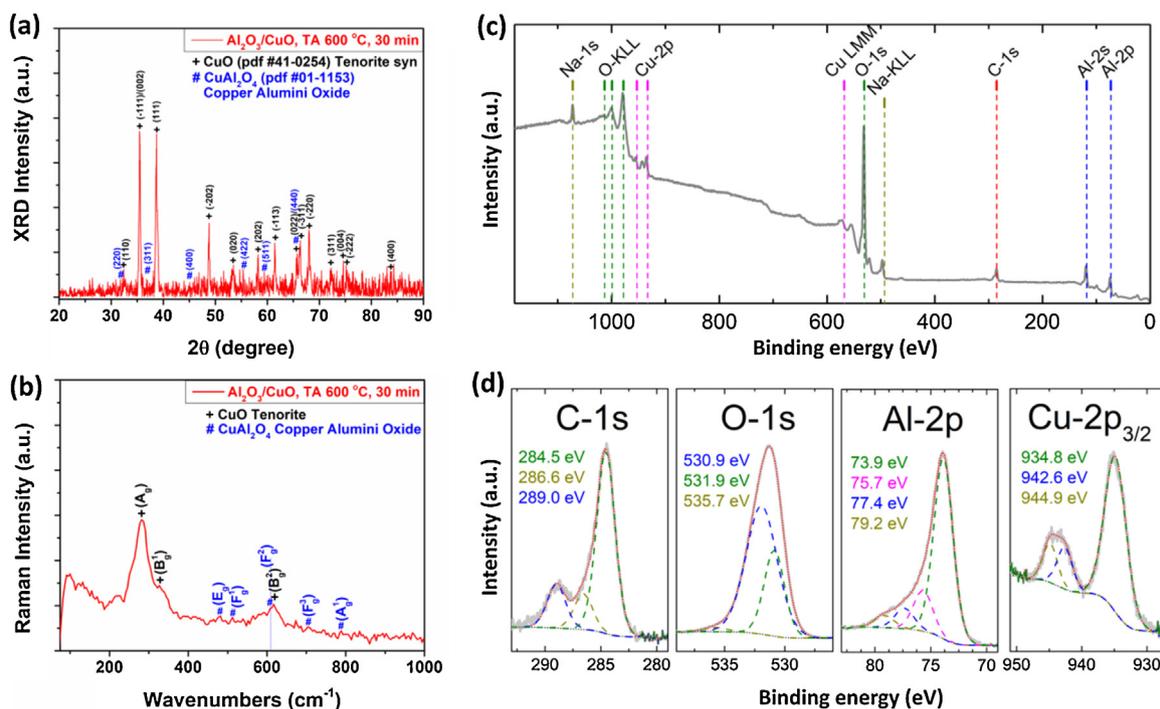
Fig. 2. (a) XRD patterns; (b) room temperature Raman spectrum; (c) XPS analysis of (6 nm Al_2O_3)/CuO heterostructures with thermal treated at 600 °C for 30 min indicates the presence of Na, Cu, O, Al and C. (d) The positions for peaks are shown by dashed lines in the survey spectrum. In the high-resolution spectra, the C1s, O1s, Al2p and Cu2p lines are fitted and dashed lines show the peak positions of the respective components.

has 12 phonon branches due to its primitive cell, so the modes are [5,55]:

$$\Gamma_{vibr} = A_g + 2B_g + 4A_u + 5B_u \tag{5}$$

where $A_u + 2B_u$ are three accoustic modes; $A_g + 2B_g$ are nine Raman-active optical modes; and $3A_u + 3B_u$ are – six IR-active modes [5,58]. The IR modes implicate the motion of Cu and O atoms and the induced dipole moment is onward of axis b for A_u modes and vertical to axis b for the B_u modes [5]. In the B_g and A_g Raman modes, the O atoms move perpendicular to the b-axis for B_g modes and in the b-direction for A_g [5,58].

The structure of $CuAl_2O_4$ is an inverse cubic spinel with space group O_h–$Fd3m$. The lattice vibrations which are active optically in different symmetry species are [50,59]:

$$\Gamma = A_{1g} + E_g + 3F_{2g} + 5F_{1u} + F_{1g} + 2A_{2u} + 2E_u + 2F_{2u} \tag{6}$$

where A_{1g}, $3F_{2g}$ and E_g are Raman-active modes; and F_{1u} are infrared-active modes. In the $5F_{1u}$ modes, one mode with zero frequency corresponds to a translation mode, but the other four modes are detected in the infra-red region. There is a single micro-Raman mode which is inactive, F_{1g}, while $2E_u$, $2A_{2u}$ and $2F_{2u}$ are inactive infrared modes. The band at ~788 cm^{-1} has been attributed to A_{1g}, showing the vibrations of M_t–O_4 tetrahedra (M_t, tetrahedral cation), bands at ~608, 512 and 703 cm^{-1} have been attributed to the F_{2g} mode, due to Cu–O vibrations, and the sluggish mode at 481 cm^{-1} has been assigned to the E_g mode, conforming to the curving mode of Al–O tetrahedral [50,51,59,60].

The XPS investigation of (6 nm Al_2O_3)/CuO heterostructures indicates the presence of Na, O, Cu, C and Al, which can be identified in the XPS survey spectrum, shown in Fig. 2(c). The signal corresponding to C stems from surface contaminations by atmospheric carbon and occurs as a result of the ALD layer, where TMA organic material, i.e. $Al(CH_3)_3$, was used as the aluminum precursor. The signal corresponding to Na, Cu and Al is attributed to the Al_2O_3/CuO heterostructures. The signal of O is partially related to atmospheric

contaminations but mainly to oxidation of Na, Cu and Al from the sample. The occurrence of a Na signal can be assigned to the uncovered surfaces or the migration/transfer of sodium ions from the substrate made of microscope glass to the (6 nm Al_2O_3)/CuO heterostructures [61–63].

A closer look at the high-resolution spectrum of the Al-2p lines, shown in Fig. 2(d), reveals that the main peak of the Al-2p line is located around 73.9 eV. Due to the limitations of the measurement set-up, it is not possible to resolve the peak splitting between Al-$2p_{3/2}$ and Al-$2p_{1/2}$. The peak location around 73.9 eV agrees well with Al^{3+} in Al_2O_3, which is commonly reported between 73.7 eV and 74.8 eV [31,64]. The occurrence of an additional shoulder, ranging from the main peak towards higher binding energies is on the one hand due to an overlap with the Cu-3p lines (typically located around 76 eV) [31] and on the other hand potentially due to the presence of a different chemical environment, e.g. in Al_2CuO_4 (typically reported between 74.2 eV and 74.7 eV) or the Al–OH bonds in for example $Al(OH)_3$ (typically reported between 74.0 eV and 75.7 eV) [31,64].

As observed in the high-resolution spectrum of the Cu-2p lines in Fig. 2(d), the peak position of the $Cu2p_{3/2}$ line is centered at ~934.8 eV, which is an indication of the presence of Cu^{2+} in CuO (typically located between 933.2 eV and 934.4 eV) rather than Cu^+ in Cu_2O (commonly reported between 932.0 eV and 932.7 eV) or metallic Cu (between 932.2 eV and 933.0 eV) [31,64–66]. Also, the occurrence of satellite peaks to the Cu-$2p_{3/2}$ line around 942.6 eV and 944.9 eV supports the assignment to Cu^{2+} in CuO.

However, based on the high sensitivity of the surface for XPS, the presence of Cu and Al in different oxidation states within the bulk of the (6 nm Al_2O_3)/CuO may not be ruled out here.

3.3. Gas sensing properties

Fig. 3(a) presents the response to various gases (hydrogen, n-butanol, ethanol, 2-propanol, acetone, carbon dioxide, methane
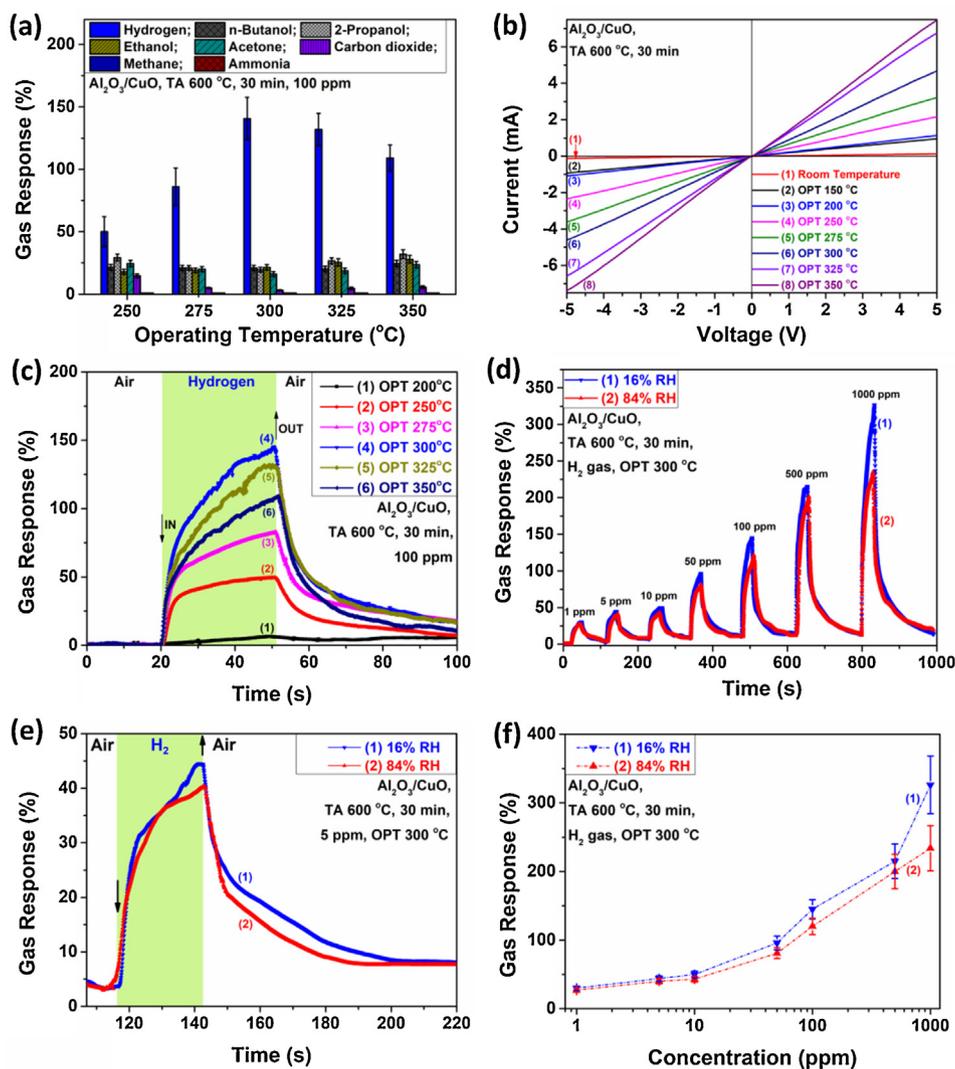
Fig. 3. (a) Gas response to various gases (100 ppm) and work temperatures of (6 nm Al_2O_3)/CuO heterostructures with thermal treated at 600 °C for 30 min. (b) I/V-characteristics for Al_2O_3/CuO heterostructures treatment treated at 600 °C for 30 min at multiple work temperatures. (c) Dynamic response to 100 ppm of hydrogen gas for (6 nm Al_2O_3)/CuO heterostructures treatment treated at 600 °C for 30 min at multiple work temperatures. (d) Dynamic response to multiple concentrations of hydrogen (1, 5, 10, 50, 100, 500 and 1000 ppm) and work temperature of 300 °C of (6 nm Al_2O_3)/CuO heterostructures treatment annealing at 600 °C for 30 min for low and high relative humidity. (e) Dynamic response to 5 ppm of hydrogen gas for (6 nm Al_2O_3)/CuO heterostructures treatment annealing at 600 °C for 30 min at OPT 300 °C. (f) Response to different concentrations of hydrogen gas at work temperature of 300 °C for low and high relative humidity.

and ammonia) with concentrations of 100 ppm by the (6 nm Al_2O_3)/CuO heterostructures at different working temperatures. The gas response shows *p*-type conductivity behavior for all tested gases, since the electrical resistance increased after the introduction of the gases. Furthermore, a high and selective response to H_2 at all working temperatures was observed. The responses are ~50 %, ~86 %, ~140 %, ~131 % and ~109 % at working temperatures of 250 °C, 275 °C, 300 °C, 325 °C and 350 °C, respectively, and the optimal operating temperature was 300 °C. For comparison, **Fig. S5(a)** shows the data for CuO nanostructures without an additional Al_2O_3 top layer (TA 600 °C for 30 min) with response/selectivity to ethanol vapors at OPT of 250 °C and to H_2 gas at higher working temperatures. Fig. 3(**b**) illustrates the characteristic current-voltage curves of (6 nm Al_2O_3)/CuO heterostructures after TA at 600 °C for 30 min at various working temperatures, i.e. an increase of the electrical current with operating temperature and proven Ohmic behavior with a linear characteristic. Fig. 3(**c**) shows the dynamic hydrogen response of (6 nm Al_2O_3)/CuO heterostructures with TA at 600 °C at various working temperatures. Response and recovery times are

τ_r = 14.5 s, 21.2 s, 18.7 s, 22.7 s and 22.8 s and τ_d = 56.1 s, 48.1 s, 56.3 s, 55.8 s, 47.1 s at working temperatures of 250 °C, 275 °C, 300 °C, 325 °C and 350 °C, respectively. Fig. 3(**d**) presents the dynamic response to different concentrations of hydrogen (1, 5, 10, 50, 100, 500 and 1000 ppm) at a working temperature of 300 °C for the (6 nm Al_2O_3)/CuO heterostructures after thermal annealing at 600 °C for 30 min under low relative humidity (16 % RH, curve 1) and high relative humidity (84 % RH curve 2). For example, a response of ~27 % is measured at 1 ppm H_2. Here, the differences in response for low and high relative humidities for 1, 5, 10, 50, 100, 500 and 1000 ppm H_2 can also be observed, indicating changes of ~10 %, ~11 %, ~13 %, ~17 %, ~16 %, ~7% and ~28 %, respectively, from the maximum response for each concentration. For a better understanding of the effect of working temperature and relative humidity on the sensors, they are plotted in **Fig. S6(a,b)** using the real values of the sensor resistance. Comparing the data obtained for (6 nm Al_2O_3)/CuO heterostructures with the CuO nanostructures in Fig. 4(**c**), the high RH leads to a reduction in the H_2 response by on average 35–40 % for CuO. Furthermore, the response to ethanol vapor (**Fig. S5(b)**)
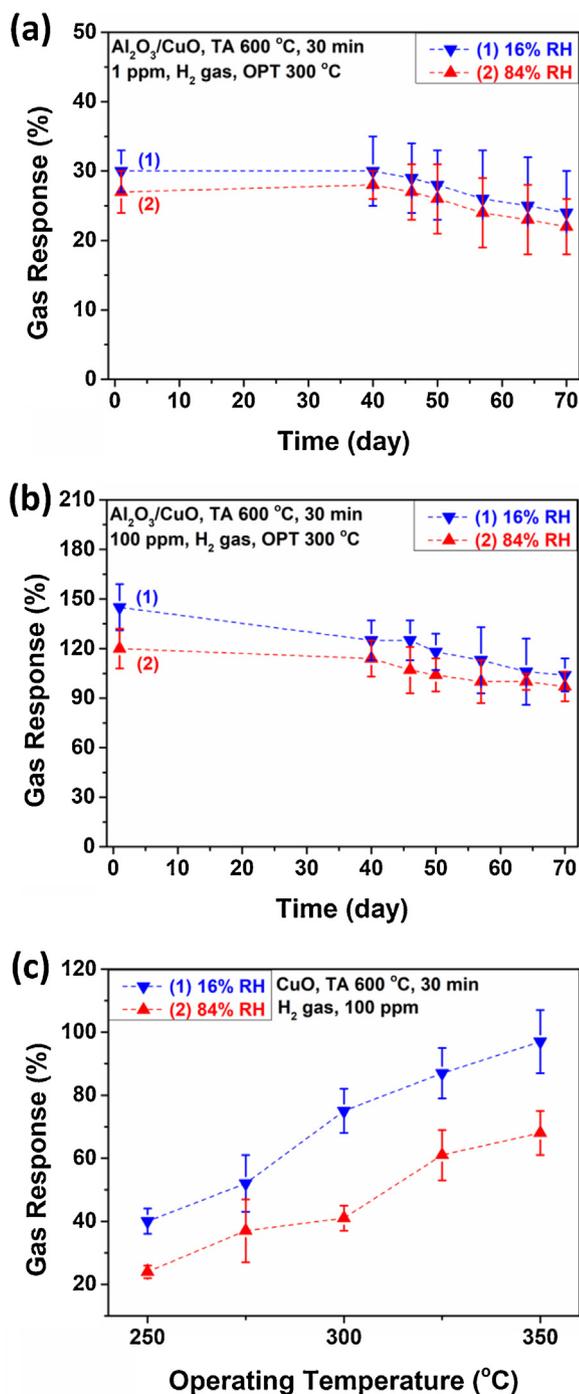
Fig. 4. The long-term stability of (6 nm Al$_2$O$_3$)/CuO heterostructures for low and high relative humidity at work temperature of 300 °C and the response to H$_2$ gas with concentrations of: (a) 1 ppm; and (b) 100 ppm. (c) Response to H$_2$ gas versus operating temperatures for low and high relative humidity of CuO nanostructures.

is drastically decreased at high RH, resulting in an approximately zero response. In contrast, the (6 nm Al$_2$O$_3$)/CuO heterostructures demonstrate excellent stability at the high relative humidity.

The error bars express the maximum and minimum values of the response measured from four tested sensor sets of each heterostructure at given concentrations of vapors exposed to 16 % and 84 % RH (see **Fig. 3(f)**). **Fig. 3(e)** exhibits the dynamic gas response to 5 ppm of hydrogen for 6 nm Al$_2$O$_3$/CuO heterostructures at an OPT of 300 °C. Here, the effect of the relative humidity on the sensing of low concentrations of hydrogen gas is negligible. **Fig. 3(f)** displays the gas response versus concentration of hydrogen gas from 1 ppm

to 1000 ppm at an OPT of 300 °C. At lower concentrations of test gases, the response is high and increases with higher concentration; in addition, at high relative humidity an increased stability is observable. This might be explained by the high aspect ratio and conformal coverage of the deposited nano-layer (5–6 nm) of Al$_2$O$_3$ on *p*-type CuO grains compared to the unprotected structure, which does not affect the surface-area-to-volume-ratio, but the surface chemistry.

The dynamic response to multiple types of vapors at a working temperature of 300 °C of the (6 nm Al$_2$O$_3$)/CuO heterostructures is displayed in **Fig. S7(a)**, indicating high selectivity to hydrogen gas. The dynamic response with three consecutive pulses to hydrogen with 100 ppm gas concentration at a working temperature of 300 °C of (6 nm Al$_2$O$_3$)/CuO heterostructures after thermal treatment at 600 °C during 30 min is presented in **Fig. S7(b)**. Here, the superior sensing performances, with excellent repeatability, make this system highly useful for practical applications and for the development of real devices.

Fig. 4(a,b) show the long-term stability of (6 nm Al$_2$O$_3$)/CuO heterostructures under low (16 %) and high (84 %) relative humidity and the response over 70 days to H$_2$ gas at a working temperature of 300 °C with concentrations of 1 ppm (**Fig. 4(a)**) and 100 ppm (**Fig. 4(b)**). We note, that after 70 days the gas response is approximately constant, varying by only 10–15 %, demonstrating the long-term stability of the sensors. The long-term stability toward H$_2$ gas with concentrations of 5 ppm from **Fig. S8** shows approximately the same stability within 10 %. **Fig. 4(c)** shows the response to H$_2$ gas versus various working temperatures for low and high relative humidity of CuO nanostructures after thermal annealing at 600 °C for 30 min. Here, the high RH leads to a reduction in the H$_2$ response by 35–40 %.

Fig. 5(a) shows the gas response to various gases (hydrogen, *n*-butanol, 2-propanol, ethanol, acetone and ammonia) with a concentration of 100 ppm for (15 nm Al$_2$O$_3$)/CuO heterostructures after thermal annealing at 620 °C for 40 min. **Fig. 5(a)** shows that, independent of the working temperatures (275 °C, 300 °C, 325 °C and 350 °C), the sample is selective to hydrogen gas with response values of ∼51 %, ∼54 %, ∼61 % and ∼75 %, respectively. **Fig. 5(b)** shows the current-voltage characteristic of (15 nm Al$_2$O$_3$)/CuO heterostructures after TA 620 °C during 40 min at different operating temperatures. The samples show Ohmic behavior with a linear characteristic and the current decreases with the operating temperature compared to the (6 nm Al$_2$O$_3$)/CuO sample (**Fig. 3(b)**), possibly due to the thicker layer (15 nm) of Al$_2$O$_3$. **Fig. 5(c)** shows the dynamic response to hydrogen of (15 nm Al$_2$O$_3$)/CuO heterostructures after TA at 620 °C for 40 min at different operating temperatures, with values of τ_r = 17.4 s, 18.3 s, 19.7 s, 20.8 s and τ_d = 61.3 s, 63.2 s, 60.1 s, 59.9 s for the response and recovery times at working temperatures of 275 °C, 300 °C, 325 °C and 350 °C, respectively.

Fig. 5(d) presents the dynamic response to multiple concentrations of hydrogen (1, 5, 10, 50, 100, 500 and 1000 ppm) at a working temperature of 350 °C of (15 nm Al$_2$O$_3$)/CuO heterostructures after thermal annealing at 620 °C for 40 min for low RH (curve 1) and high RH (curve 2).

It can be observed that the high RH does not affect the sensor even at low hydrogen concentrations (1 ppm), where a 9 % response was obtained (see **Fig. 5(e)**). Whereas for the (6 nm Al$_2$O$_3$)/CuO sample (**Fig. 3(d)**) at high relative humidity the response is still affected by 10–15 %, the (15 nm Al$_2$O$_3$)/CuO sample show no change in the response. **Fig. 5(f)** shows the gas response versus concentration of hydrogen gas from 1 ppm to 1000 ppm at an OPT of 350 °C. At relatively low concentrations, the response is high and increases with higher concentrations. In addition, at high relative humidity the increased stability is observable, which might be explained by
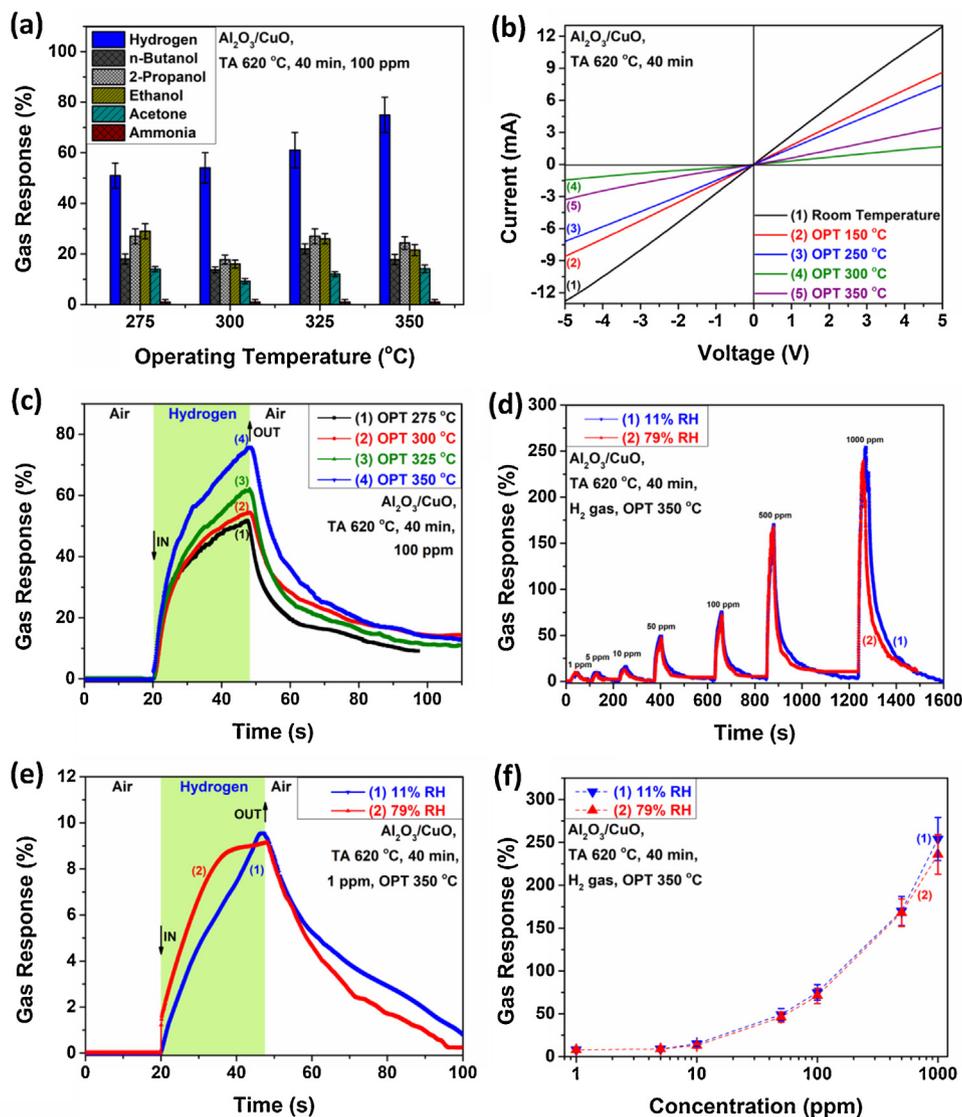
Fig. 5. (a) Gas response to various gases (100 ppm) and work temperatures of (15 nm Al_2O_3)/CuO heterostructures with thermal annealing at 620 °C for 40 min. (b) I/V-characteristics for (15 nm Al_2O_3)/CuO heterostructures with thermal annealing at 620 °C for 40 min at different operating temperatures. (c) Dynamic response to 100 ppm of hydrogen gas for (15 nm Al_2O_3)/CuO heterostructures with thermal annealing at 620 °C for 40 min at different operating temperatures. (d) Dynamic response to different concentrations of hydrogen (1, 5, 10, 50, 100, 500 and 1000 ppm) and work temperature of 350 °C of (15 nm Al_2O_3)/CuO heterostructures with thermal annealing at 620 °C for 40 min for low and high relative humidity. (e) Dynamic response to 1 ppm of hydrogen gas for (15 nm Al_2O_3)/CuO heterostructures with thermal annealing at 620 °C for 40 min at OPT 300 °C. (f) Response to multiple concentrations of hydrogen gas at work temperature of 350 °C for low and high relative humidity.

the high aspect ratio conformal coverage of the deposited thicker nano-layer (15 nm) of Al_2O_3 on *p*-type CuO grains.

The gas detection studies of nano-Al_2O_3/CuO heterostructures, showing the high selectivity for H_2 gas, the stability in long-term usage, stability under humidity, as well as the detection of very low concentrations of only 1 ppm, suggest that an important application field could be the monitoring of thermal runaway in Li-ion-batteries (LIBs). LIBs with a critical failure (short circuit, damage, etc.) can trigger a chain of exothermic reactions that leads to a rapid rise in temperature and consequent catastrophic self-accelerated degradation (thermal runaway) of the LIB with the elimination of hydrogen and hydrocarbons [67]. Moreover, hydrogen is one of the most common gases found in LIB, after long-term cycling and/or storage at elevated/high temperatures [68]. H_2 gas production in LIBs is assigned to residual moisture, due to insufficient drying of the electrodes, separators and other cell components. Even small amounts of H_2O contamination inside

the electrolyte can lead to multiple electrolyte degradation and corrosion reactions at the electrode/electrolyte interfaces [68–70]. Applying nano-Al_2O_3/CuO heterostructures sensors close to individual battery cells could identify units that are failing from the H_2 gas eliminated, thus indicating probable thermal runaway that can heat LIBs to over 200 °C by ensuring the appropriate working temperature for the sensor.

The selective detection of hydrogen, moisture stability and detection of low hydrogen concentrations by sensors based on nano-Al_2O_3/CuO heterostructures, makes their integration in the vicinity of the individual battery cells an attractive prospect, i.e. over the connecting busbars of battery cells [71], or above the battery cell [72]. Thus, a possible route to an efficient and rapid sensing of the very early phase of thermal runaway could be achieved, thereby avoiding the degradation of other parallel connected cell units.
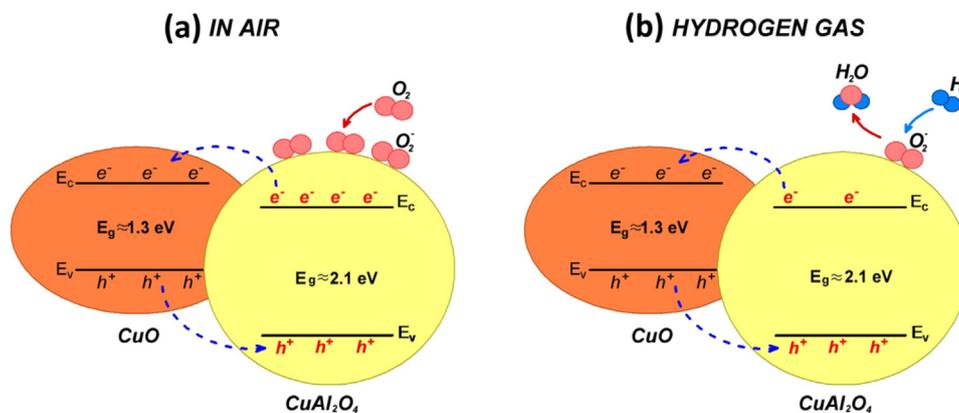
Fig. 6. Schematic illustration of the H_2 detecting mechanism for $CuAl_2O_4$/CuO heterostructure: (a) under ambient atmosphere; and (b) under hydrogen gas.

3.4. Proposed gas detection mechanism

The mechanism for gas detection of heterostructure-based nanomaterials is still under debate. The main gas and vapor sensing models for *p*-type conductometric devices are explained as molecular adsorption, followed by a charge transfer directly between the gaseous molecules and heterostructure-based nanomaterials to produce modulation of the Fermi level, i.e. variation in the electrical conductivity. The basic gas sensing-detection mechanism of our heterojunctions can be discussed following the existing models of ionosorption [73–78].

(Co, Ni, Cu, Zn) aluminate is known as a catalytic material with a low acidity for surfaces, but high thermal and chemical stabilities for growth, hydrogenation, dehydrogenation, dehydration, isomerization and combustion processes [79–82].

As such, the response enhancement for H_2 could be interpreted as depending on the free electron and hole transfer and the charge separation owing to the $CuAl_2O_4$/CuO nano-hetrostructure. The creation of *n-p* and *n-n* nano-heterojunctions is known to be highly valuable in improving detection characteristics [2,73–77,83].

Fig. 6 presents a schematic of the H_2 detection suggested for a $CuAl_2O_4$/CuO structure. A flow of electrons will leak from $CuAl_2O_4$ nanodots to the CuO nanostructure that is formed following the thermal annealing of Al_2O_3 at a temperature of 600 °C (see Fig. 1(**a–d**)), thereby producing an increase in the hole concentration in the $CuAl_2O_4$ surrounding nanodots. This situation will lead to a higher coverage of oxygen species on the $CuAl_2O_4$ nano-island-dot surfaces in air (Fig. 6(**a**)), provoking higher hole concentrations in that region, thus improving reactions on the surface, e.g. the absorption of a test gas if the heterostructure was exposed to gas. Upon application of hydrogen gas (Fig. 6(**b**)), adsorption and reaction with oxygen will take place, enhancing the response, based on a smaller charge transfer value on the top surface [2,73,80,84].

The detection steps suggested here illustrate that the existence of $CuAl_2O_4$ will enhance the adsorption of species on the $CuAl_2O_4$ surface, because transfer of free charge carriers from CuO to $CuAl_2O_4$ will speed up the oxidation processes. The improvement of surface reactions such as adsorption, dissociation, and the ionization of oxygen through the presence of different nano-particles of metal oxides, for example NiO and In_2O_3, has been recognized previously [85,86].

At operating temperatures of 250–350 °C in ambient air (the ranges of temperature involved for current investigation), the adsorbed species on the surface of metal oxides is principally molecular oxygen (O_2), which takes a free hole in a top surface state, (see Fig. 6(**a**)) according to the equation [73,78,80,87]:

$$O_{2(gas)} \rightarrow O_{2(ads)} + h^+ \rightarrow O_{2(ads)}^- \tag{7}$$
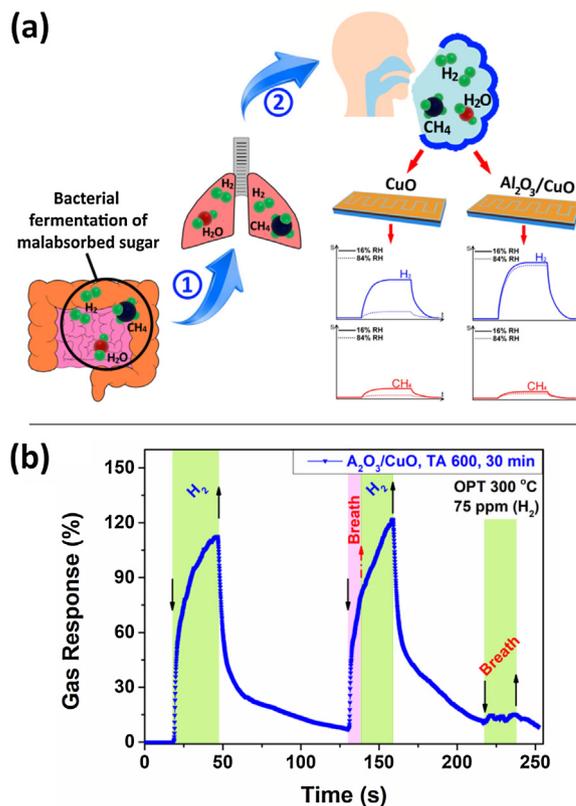
Fig. 7. (a) Schematic of principle of hydrogen and/or methane breath test; (b) the influence of breath from a healthy person on the hydrogen response.

For hetero-structures, this process will contribute to the appearance of a depletion region at the top of the surface.

Next, upon exposure to hydrogen gas the following reaction takes place [21,83,88,89]:

$$2H_{2(gas)} + O_{2(ads)}^- + h^+ \rightarrow 2H_2O + Null \tag{8}$$
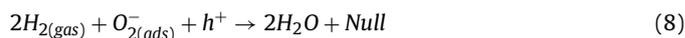
Two H_2O molecules are formed and the holes in the depleted region will recombine with the released electrons forming Null ($h^+ + e^- \rightarrow Null$). Next occurs a narrowing of the depletion region and a decrease in the electrical current or an increase in the resistance of the heterostructure.
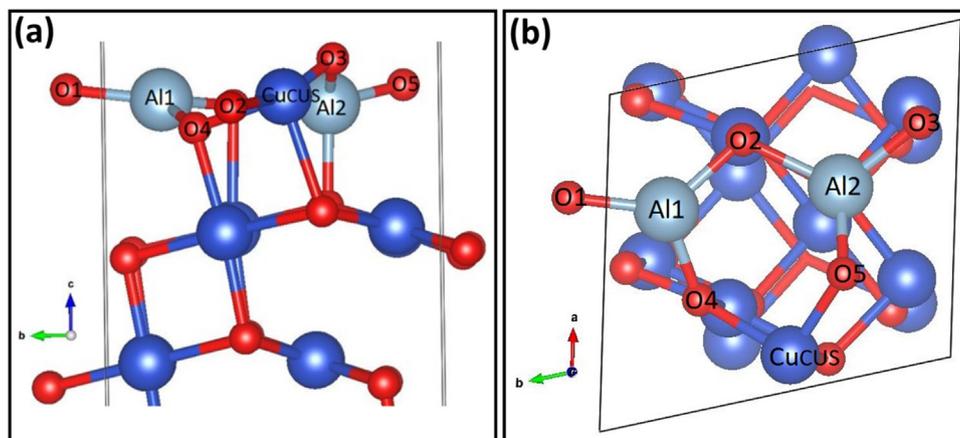
Fig. 8. Side (a) and top view (b) of the relaxed structure of the Al_2O_3-CuO (111) surface, where O = red, Al = light blue, and Cu = dark blue.

3.5. Breath test sensing

Fig. 7(**a**) illustrates schematically the principle of a hydrogen and/or methane breath test. Initially, bacterial fermentation of a badly absorbed sugar takes place in the intestines, where hydrogen and/or methane gas is produced. Thus, hydrogen and/or methane gas is absorbed into the bloodstream and transported to the lungs (see Fig. 7(**a**), step 1). Upon these gases from the blood flow reaching the lungs, they are transported by exhalation (see Fig. 7(**a**), step 2). The breath can be analyzed, representing a very useful non-invasive investigation method. In our case, the breath tests were performed as follows: at the working temperature of 300 °C, first a flow of H_2 gas with a concentration of 75 ppm was applied to the sample; at the same time as the H_2 gas, an expiration of air from a person was applied for 10 s to obtain the second pulse in Fig. 7(**b**); whereas the third pulse in this figure is obtained solely from the expiration of air from a person to see the influence of the response on breath dependence. Fig. 7(**b**) shows the effect of breath on the hydrogen response. It can be seen that the first pulse, where only hydrogen gas is applied with a concentration of 75 ppm at a working temperature of 300 °C, leads to a response of 112 %. A second pulse, applied for 10 s and composed of 75 ppm of hydrogen gas and a test-breath, leads to a maximum response of 121 %. Here, the test-breath showed no effect on the response, which proves the excellent stability of the sensor. Only in the third pulse, upon application of the test-breath only, a negligible response of about 5% is shown, explaining the high response to the second pulse of 121 %. For comparison, **Fig. S9** shows the effect of breath on the hydrogen response under longer exposure of 25 s, when 75 ppm of hydrogen gas is applied in the second pulse. This also had low impact on the sensing performance.

3.6. DFT calculations: H_2 molecule interaction with Al_2O_3-CuO (111) surface

The (111) surface was found to be the dominant plane in the CuO morphology, with the lowest surface energy of 0.75 J/m² [44]. The atomic top-layer of the CuO (111) surface contains two 3- and two 4-coordinated copper and oxygen atoms. 3-coordinated Cu_{CUS} are coordinatively unsaturated atoms, and 4-coordinated Cu_{CSA} are coordinatively saturated copper atoms, both present in the top layer (see **Fig. S10**). O_{SUF} are the most exposed 3-coordinated oxygen atoms, whereas O_{SUB} are 4-coordinated sub-surface oxygen atoms. We first relaxed the surface with the optimized geometry shown in **Fig. S10**. In order to model the Al_2O_3:CuO (111) surface, we replaced 3 Cu atoms with 2 Al atoms to maintain charge neutrality and while replacing, we considered both the top surface layer

as well as the second Cu-O layer. Different configurations were investigated by substitution of various copper atoms in the first and second layers and we found the lowest energy structure to be one, where we had removed one 4-coordinated copper (Cu_{CSA}) atom from the top layer and substituted one 4-coordinated (Cu_{CSA}) and one 3-coordinated (Cu_{CUS}) atom with Al atoms. After relaxation, we noted that one of the aluminum atom, Al1, which was substituted for the 4-coordinated copper atom Cu_{CSA}, binds to three oxygen atoms in the top surface layer, whereas the second Al atom, Al2, which was substituted for a 3-coordinated copper atom, Cu_{CUS}, forms four Al-O bonds in the topmost surface layer, as shown in Fig. 8. As such, we observed presence of one Cu, two Al atoms bonded with four oxygen atoms in the top surface layer, resulting in $CuAl_2O_4$/CuO heterostructure formation of a $CuAl_2O_4$/CuO heterostructure in the top layer of the surface, with Al-O bond lengths ranging from 1.711 Å to 1.884 Å.

We next placed a H_2 molecule in various orientations close to different surface sites and noted that upon geometry optimisation the molecule dissociates spontaneously, with one H atom binding to one of the surface oxygen atoms that is bonded to a surface Al atom and a second layer Cu atom, with the other H atom binding to another surface O atom that was shared between the second Al atom and a Cu_{CUS} atom in the top layer, as shown in Fig. 9. On adsorption, the surface Al-O and Cu-O bond lengths increase, with the Al1-O4 bond elongating from 1.73 Å to 1.80 Å, the Al2-O5 bond length increasing from 1.71 Å to 1.80 Å and Cu_{CUS}-O5 increasing to 1.94 Å from its original value of 1.81 Å.

In order to further asses the interaction of the hydrogen molecule with the Al_2O_3-CuO (111) surface, we performed a Bader charge analysis and plotted the charge density difference, as shown in Fig. 9(**b**). We note that because of the interaction with surface Al and Cu atoms, both hydrogen atoms lose charge density to gain positive charges of 0.68 and 0.70 e⁻ respectively, whereas the Bader charges of Al1, Al2 and the surface Cu atom, which bind the hydrogen atoms, change from 2.37, 2.41 and 1.09 e⁻ to 2.36, 2.43 and 0.526 e⁻, respectively. In order to further quantify the electronic structure changes, we have also calculated the electronic density of states (DOS) and the results show that there is considerable shift in the conduction band, as the band gap changes from 0.88 eV to 1.09 eV (see Fig. 10).

The change in electronic states is also reflected in the Fermi energy, which changes from -1.808 to -1.147 eV as a result of the interaction of the hydrogen gas with the Al_2O_3:CuO surface. The binding energy for the dissociated H_2 molecule is calculated to be -2.83 eV.

The dissociative adsorption of the H_2 molecule on the Al_2O_3:CuO surface is in contrast to the behavior on the pristine CuO (111) top
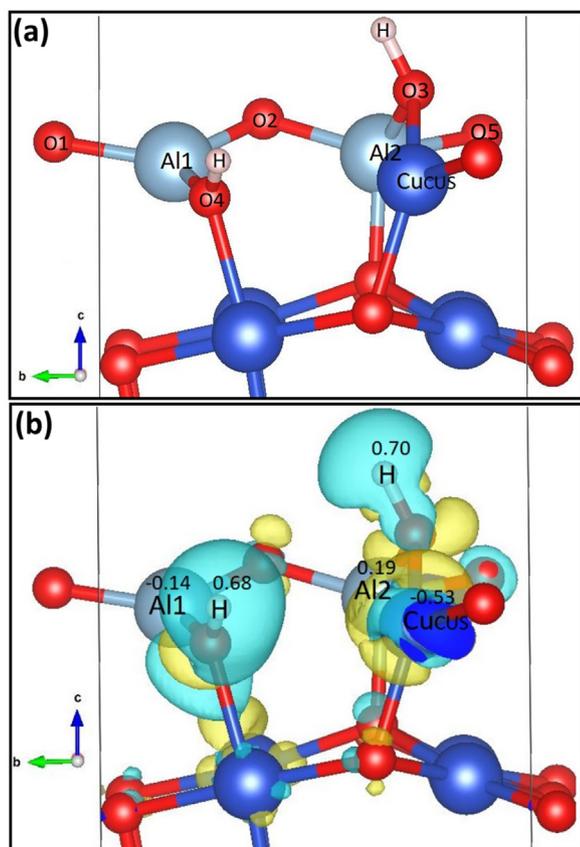
Fig. 9. (a) Interaction of Hydrogen molecule with Al_2O_3-CuO (111) surface. Hydrogen atoms are shown in salmon pink, whereas the colour scheme of the other atoms is the same as in Fig. 8; (b) Charge density difference plot of H_2 molecule interaction on the Al_2O_3-CuO (111) surface, where positive and negative charge densities in (e/Bohr^3) are indicated by yellow and blue colours. Different numbers indicate bader charges on aroms. Colour scheme for the atoms is the same as in (a).

Fig. 10. Density of states of (a) the Al_2O_3-CuO(111) surface, and (b) the system of the Hydrogen molecule adsorbed on the Al_2O_3-CuO(111) surface.

Fig. 11. H_2O molecule interaction with Al_2O_3-CuO (111) surface. Hydrogen atoms are represented by salmon pink colour, while other atoms colour sheme is same as in Fig. 8.

surface, where we have established that the H_2 molecule forms an adsorbed water molecule through binding to the most exposed O atoms at the CuO (111) surface, thereby reducing the CuO (111) surface [90]. We have also investigated the interaction of the hydrogen molecule with the tenorite (111) top surface with a lower level of Al doping, where we used a 2 × 2 surface simulation cell of CuO (111), consisting of 64 Cu and 64 O atoms, and replaced 3 top layer Cu atoms by 2 Al atoms. Similar to the 1 × 1 cell, we selected the configuration with the lowest energy, i.e. where we had replaced two 4-coordinated copper (Cu_{CSA}) atoms and one 3-coordinated (Cu_{CUS}) atom by Al atoms. We next placed a H_2 molecule onto the surface, but observed similar dissociative adsorption of the H_2 molecule, as presented in **Fig. S11**.

To investigate the role of water on the Al_2O_3-CuO (111) surface, we next studied the interaction of an H_2O molecule, again by placing the molecule in different orientations close to Al-Cu heterostructure formed as a result of Al doping of the CuO (111) surface. We noted that the H_2O molecule dissociates into H and OH species which bind to the surface (see Fig. 11). The OH species binds to one of the aluminum atoms, Al1, with a bond length of 1.768 Å, while the H atom binds to one of the surface oxygen atoms, shared between the second Al atom (Al2) and a copper Cu_{CUS} atom. Again, this behavior is in contrast to the interaction of a water molecule with the pristine CuO (111) surface, where no such dissociation is observed and the molecule binds instead to an unsaturated copper atom, Cu_{CUS} (d_{Cu-O} =2.08 Å), as show in **Fig. S12**.

4. Conclusions

In this work, we have reported the synthesis of nano-Al_2O_3/CuO heterostructures with low sensitivity to humidity and an increased ratio in H_2/humidity interference/sensitivity. The proposed method allows the elimination of the effects of humidity in the response to gases by conductometric chemical-sensitive heterostructures, via the use of an ultra-thin oxide layer formed on top of the surface through high-aspect ratio ALD. A 6 nm Al_2O_3 nano-layer was grown on top of the surface of CuO nanostructures thus obtaining a nano-Al_2O_3/CuO heterostructure, which resulted in the formation of a heterojunction of $CuAl_2O_4$ and CuO after treatment at 600 °C for 30 min, as shown by XRD and Raman measurements. The sensor system demonstrated a high selectivity to H_2 gas with a value of ~140 %, at operating temperatures of about 300 °C. Fur-

thermore, the ability to detect small concentrations of hydrogen gas was demonstrated, obtaining a response of ~27 % to a concentration of only 1 ppm, as well as a stabilizing effect at high concentrations of relative humidity. The response at 84 % RH was modified by only ~10 % from the response value at 16 % RH, which can be explained on the basis of higher aspect ratio coverage of p-type CuO compared to the unprotected material. The DFT calculations have revealed the fundamentally different behavior between the Al_2O_3:CuO heterostructure and the CuO (111) surface. The H_2 molecule interacts strongly with the Al_2O_3:CuO (111) surfaces by dissociating into atomic hydrogens and binding to Al-bound surface oxygen atoms, in contrast with the behavior of H_2 molecules on the pristine CuO (111) surfaces, where an adsorbed water molecule is known to form surface-bound water, due to the H_2 molecule interacting with surface oxygen atoms. Furthermore, owing to the more reactive nature of the Al-CuO heterostructure, the spontaneous dissociation of water molecules is also observed over this Al_2O_3:CuO surface, again in contrast to the pure CuO (111) surface where water adsorbs molecularly.

A study into the effect of thermal annealing temperatures and durations, with respect to RH and H_2 concentrations as well as temperature, is in progress and will be published elsewhere. Our advances in such a competitive field could contribute to the development of a cost-effective, low-power heterostructure for widespread detection of H_2 in portable battery applications, not only for gas analysis, but also for security, environmental, breath test and food safety applications.

Author Contributions

O.L., N.A., S.H., F.F., A.K.M. and R.A. conceptualization of this study and design. N.A., O.L., B.W. and M.T.B. synthesized the material and developed the synthesis-treatment methodology. A.V. and F.F. carried out XPS measurements and XPS data analysis. H.K. and S.H. carried out battery investigations and write-up. O.L., N.A. and R.A. carried out all Raman experiments and data discussion. O.L., N.A. and S.H. fitted a technology pathway for material integrations in the devices. N.A., N.M., O.L. performed the measurements of the sensor characteristics of the materials and investigated the data. O.L., N.A., N.M., S.H., R.A., H.K., B.W. and M.T.B. analyzed the experimental data/results, then the revised work. N.H.L. and A.K.M. accomplished the computational and DFT draft. A.K.M. and N.H.L. performed and analyzed the computational results. O.L., N.A., H.K., A.K.M. and N.H.L.: Writing- Reviewing and Editing. O.L., N.A., M.T.B., S.H., A.V, F.F. and R.A. prepared the manuscript draft. S.H. and R.A.: Supervision. All gave the approval of the final version for manuscript to be submitted. This work was written based on all authors contributions. All of our co-authors reviewed the draft and have given approval to the final version of the manuscript.

Declaration of Competing Interest

The authors declare that they have no known competing financial interests or personal relationships that could have appeared to influence the work reported in this paper.

The authors report no declarations of interest.

Acknowledgment

Appendix A. Supplementary data

Supplementary material related to this article can be found, in the online version, at doi:https://doi.org/10.1016/j.sna.2021.112804.

References

[1] D. Zappa, V. Galstyan, N. Kaur, H.M.M. Munasinghe Arachchige, O. Sisman, E. Comini, Metal oxide -based heterostructures for gas sensors A review, Anal. Chim. Acta 1039 (2018) 1–23, http://dx.doi.org/10.1016/j.aca.2018.09.020.

[2] D.R. Miller, S.A. Akbar, P.A. Morris, Nanoscale metal oxide-based heterojunctions for gas sensing: a review, Sens. Actuators B Chem. 204 (2014) 250–272, http://dx.doi.org/10.1016/j.snb.2014.07.074.

[3] E. Kanazawa, G. Sakai, K. Shimanoe, Y. Kanmura, Y. Teraoka, N. Miura, N. Yamazoe, Metal oxide semiconductor N_2O sensor for medical use, Sens. Actuators B Chem. 77 (2001) 72–77, http://dx.doi.org/10.1016/S0925-4005(01)00675-X.

[4] G. Korotcenkov, Metal oxides for solid-state gas sensors: What determines our choice? Mater. Sci. Eng. B 139 (2007) 1–23, http://dx.doi.org/10.1016/j.mseb.2007.01.044.

[5] V. Cretu, V. Postica, A.K. Mishra, M. Hoppe, I. Tiginyanu, Y.K. Mishra, L. Chow, N.H. de Leeuw, R. Adelung, O. Lupan, Synthesis, characterization and DFT studies of zinc-doped copper oxide nanocrystals for gas sensing applications, J. Mater. Chem. A Mater. Energy Sustain. 4 (2016) 6527–6539, http://dx.doi.org/10.1039/C6TA01355D.

[6] M. Hübner, C.E. Simion, A. Tomescu-Stănoiu, S. Pokhrel, N. Bârsan, U. Weimar, Influence of humidity on CO sensing with p-type CuO thick film gas sensors, Sens. Actuators B Chem. 153 (2011) 347–353, http://dx.doi.org/10.1016/j.snb.2010.10.046.

[7] A.R. Hopkins, N.S. Lewis, Detection and classification characteristics of arrays of carbon Black/Organic polymer composite chemiresistive vapor detectors for the nerve agent simulants dimethylmethylphosphonate and diisopropylmethylphosponate, Anal. Chem. 73 (2001) 884–892, http://dx.doi.org/10.1021/ac0008439.

[8] D.S. Vlachos, P.D. Skafidas, J.N. Avaritsiotis, The effect of humidity on tin-oxide thick-film gas sensors in the presence of reducing and combustible gases, Sensors Actuators B Chem. 25 (1995) 491–494, http://dx.doi.org/10.1016/0925-4005(95)85105-4.

[9] S.S. Nair, N. Illyaskutty, B. Tam, A.O. Yazaydin, K. Emmerich, A. Steudel, T. Hashem, L. Schöttner, C. Wöll, H. Kohler, H. Gliemann, ZnO@ZIF-8: Gas sensitive core-shell hetero-structures show reduced cross-sensitivity to humidity, Sensors Actuators B Chem. 304 (2020), 127184, http://dx.doi.org/10.1016/j.snb.2019.127184.

[10] Y. Seekaew, W. Pon-On, C. Wongchoosuk, Ultrahigh selective room-temperature Ammonia gas sensor based on tin–Titanium Dioxide/reduced Graphene/Carbon nanotube nanocomposites by the solvothermal method, ACS Omega 4 (2019) 16916–16924, http://dx.doi.org/10.1021/acsomega.9b02185.

[11] G. Konvalina, H. Haick, Effect of humidity on nanoparticle-based chemiresistors: a comparison between synthetic and real-world samples, ACS Appl. Mater. Interfaces 4 (2012) 317–325, http://dx.doi.org/10.1021/am2013695.

[12] N. Garg, A. Mohanty, N. Lazarus, L. Schultz, T.R. Rozzi, S. Santhanam, L. Weiss, J.L. Snyder, G.K. Fedder, R. Jin, Robust gold nanoparticles stabilized by trithiol for application in chemiresistive sensors, Nanotechnology. 21 (2010), 405501, http://dx.doi.org/10.1088/0957-4484/21/40/405501.

[13] N. Gupta, H.M. Fahad, M. Amani, X. Song, M. Scott, A. Javey, Elimination of response to relative humidity changes in Chemical-Sensitive field-effect transistors, ACS Sens. 4 (2019) 1857–1863, http://dx.doi.org/10.1021/acssensors.9b00637.

[14] S.V. Rana, A. Malik, Hydrogen breath tests in gastrointestinal diseases, Indian J. Clin. Biochem. 29 (2014) 398–405, http://dx.doi.org/10.1007/s12291-014-0426-4.

[15] B. Haderstorfer, D. Psycholgin, W.E. Whitehead, M.M. Schuster, Intestinal gas production from bacterial fermentation of undigested carbohydrate in irritable bowel syndrome, Am. J. Gastroenterol. 84 (1989) 375–378, http://dx.doi.org/10.1111/j.1572-0241.1989.tb02530.x.

[16] M. Pimentel, Breath Testing for Small Intestinal Bacterial Overgrowth: Should We Bother? Am. J. Gastroenterol. 111 (2016) 307–308, http://dx.doi.org/10.1038/ajg.2016.30.

[17] R. Khoshini, S.-C. Dai, S. Lezcano, M. Pimentel, A systematic review of diagnostic tests for small intestinal bacterial overgrowth, Dig. Dis. Sci. 53 (2008) 1443–1454, http://dx.doi.org/10.1007/s10620-007-0065-1.

[18] H.-T. Wang, T.J. Anderson, B.S. Kang, F. Ren, C. Li, Z.-N. Low, J. Lin, B.P. Gila, S.J. Pearton, A. Osinsky, A. Dabiran, Stable hydrogen sensors from AlGaN/GaN heterostructure diodes with TiB_2-based Ohmic contacts, Appl. Phys. Lett. 90 (2007), 252109, http://dx.doi.org/10.1063/1.2751107.

[19] H. Gu, Z. Wang, Y. Hu, Hydrogen gas sensors based on semiconductor oxide nanostructures, Sensors. 12 (2012) 5517–5550, http://dx.doi.org/10.3390/s120505517.

[20] O. Lupan, V. Postica, T. Pauporté, B. Viana, M.-I. Terasa, R. Adelung, Room temperature gas nanosensors based on individual and multiple networked Au-modified ZnO nanowires, Sensors Actuators B Chem. 299 (2019), 126977, http://dx.doi.org/10.1016/j.snb.2019.126977.

[21] O. Lupan, V.V. Ursaki, G. Chai, L. Chow, G.A. Emelchenko, I.M. Tiginyanu, A.N. Gruzintsev, A.N. Redkin, Selective hydrogen gas nanosensor using individual ZnO nanowire with fast response at room temperature, Sensors Actuators B Chem. 144 (2010) 56–66, http://dx.doi.org/10.1016/j.snb.2009.10.038.

[22] Q. Qi, T. Zhang, X. Zheng, H. Fan, L. Liu, R. Wang, Y. Zeng, Electrical response of Sm_2O_3-doped SnO_2 to C_2H_2 and effect of humidity interference, Sensors Actuators B Chem. 134 (2008) 36–42, http://dx.doi.org/10.1016/j.snb.2008.04.011.

[23] J. Gong, Q. Chen, M.-R. Lian, N.-C. Liu, R.G. Stevenson, F. Adami, Micromachined nanocrystalline silver doped SnO_2 H_2S sensor, Sensors Actuators B Chem. 114 (2006) 32–39, http://dx.doi.org/10.1016/j.snb.2005.04.035.

[24] O. Lupan, V. Postica, N. Wolff, J. Su, F. Labat, I. Ciofini, H. Cavers, R. Adelung, O. Polonskyi, F. Faupel, L. Kienle, B. Viana, T. Pauporté, Low-temperature solution synthesis of Au-Modified ZnO nanowires for highly efficient hydrogen nanosensors, ACS Appl. Mater. Interfaces 11 (2019) 32115–32126, http://dx.doi.org/10.1021/acsami.9b08598.

[25] S. Wicker, M. Guiltat, U. Weimar, A. Hémeryck, N. Barsan, Ambient Humidity Influence on CO Detection with SnO_2 Gas Sensing Materials. A Combined DRIFTS/DFT Investigation, J. Phys. Chem. C. 121 (2017) 25064–25073, http://dx.doi.org/10.1021/acs.jpcc.7b06253.

[26] C. Wang, L. Yin, L. Zhang, D. Xiang, R. Gao, Metal oxide gas sensors: sensitivity and influencing factors, Sensors. 10 (2010) 2088–2106, http://dx.doi.org/10.3390/s100302088.

[27] S.Y. Park, Y.H. Kim, S.Y. Lee, W. Sohn, J.E. Lee, D.H. Kim, Y.-S. Shim, K.C. Kwon, K.S. Choi, H.J. Yoo, J.M. Suh, M. Ko, J.-H. Lee, M.J. Lee, S.Y. Kim, M.H. Lee, H.W. Jang, Highly selective and sensitive chemoresistive humidity sensors based on rGO/MoS_2 van der Waals composites, J. Mater. Chem. A. 6 (2018) 5016–5024, http://dx.doi.org/10.1039/C7TA11375G.

[28] K.J. Choi, H.W. Jang, One-dimensional oxide nanostructures as gas-sensing materials: review and issues, Sensors. 10 (2010) 4083–4099, http://dx.doi.org/10.3390/s100404083.

[29] A. Gurlo, Nanosensors: towards morphological control of gas sensing activity. SnO_2, In_2O_3, ZnO and WO_3 case studies, Nanoscale 3 (2011) 154–165, http://dx.doi.org/10.1039/C0NR00560F.

[30] O. Lupan, V. Cretu, V. Postica, N. Ababii, O. Polonskyi, V. Kaidas, F. Schütt, Y.K. Mishra, E. Monaico, I. Tiginyanu, V. Sontea, T. Strunskus, F. Faupel, R. Adelung, Enhanced ethanol vapour sensing performances of copper oxide nanocrystals with mixed phases, Sensors Actuators B Chem. 224 (2016) 434–448, http://dx.doi.org/10.1016/j.snb.2015.10.042.

[31] W.F. Stickle, P.E. Sobol, K.D. Bomben, Handbook of X-ray Photoelectron Spectroscopy, MN Perkin Elmer., Eden Prairie, 1992.

[32] O. Lupan, N. Ababii, A.K. Mishra, O. Gronenberg, A. Vahl, U. Schürmann, V. Duppel, H. Krüger, L. Chow, L. Kienle, F. Faupel, R. Adelung, N.H. de Leeuw, S. Hansen, Single CuO/Cu_2O/Cu microwire covered by a nanowire network as a gas sensor for the detection of battery hazards, ACS Appl. Mater. Interfaces 12 (2020) 42248–42263, http://dx.doi.org/10.1021/acsami.0c09879.

[33] N. Helwig, M. Schüler, C. Bur, A. Schütze, T. Sauerwald, Gas mixing apparatus for automated gas sensor characterization, Meas. Sci. Technol. 25 (2014), 055903, http://dx.doi.org/10.1088/0957-0233/25/5/055903.

[34] S. Luo, Y. Shen, Z. Wu, M. Cao, F. Gu, L. Wang, Enhanced ethanol sensing performance of mesoporous Sn-doped ZnO, Mater. Sci. Semicond. Process. 41 (2016) 535–543, http://dx.doi.org/10.1016/j.mssp.2015.10.001.

[35] V. Postica, J. Gröttrup, R. Adelung, O. Lupan, A.K. Mishra, N.H. de Leeuw, N. Ababii, J.F.C. Carreira, J. Rodrigues, N. Ben Sedrine, M.R. Correia, T. Monteiro, V. Sontea, Y.K. Mishra, Multifunctional Materials: A Case Study of the Effects of Metal Doping on ZnO Tetrapods with Bismuth and Tin Oxides, Adv. Funct. Mater. 27 (2017), 1604676, http://dx.doi.org/10.1002/adfm.201604676.

[36] P.E. Blöchl, Projector augmented-wave method, Phys. Rev. B 50 (1994) 17953–17979, http://dx.doi.org/10.1103/PhysRevB.50.17953.

[37] G. Kresse, D. Joubert, From ultrasoft pseudopotentials to the projector augmented-wave method, Phys. Rev. B 59 (1999) 1758–1775, http://dx.doi.org/10.1103/PhysRevB.59.1758.

[38] G. Kresse, J. Hafner, Ab initio molecular dynamics for liquid metals, Phys. Rev. B 47 (1993) 558–561, http://dx.doi.org/10.1103/PhysRevB.47.558.

[39] G. Kresse, J. Hafner, Ab initio molecular-dynamics simulation of the liquid-metal–amorphous-semiconductor transition in germanium, Phys. Rev. B 49 (1994) 14251–14269, http://dx.doi.org/10.1103/PhysRevB.49.14251.

[40] G. Kresse, J. Furthmüller, Efficiency of ab-initio total energy calculations for metals and semiconductors using a plane-wave basis set, Comput. Mater. Sci. 6 (1996) 15–50, http://dx.doi.org/10.1016/0927-0256(96)00008-0.

[41] G. Kresse, J. Furthmüller, Efficient iterative schemes for ab initio total-energy calculations using a plane-wave basis set, Phys. Rev. B 54 (1996) 11169–11186, http://dx.doi.org/10.1103/PhysRevB.54.11169.

[42] J.P. Perdew, K. Burke, M. Ernzerhof, Generalized gradient approximation made simple, Phys. Rev. Lett. 77 (1996) 3865–3868, http://dx.doi.org/10.1103/PhysRevLett.77.3865.

[43] S.L. Dudarev, G.A. Botton, S.Y. Savrasov, C.J. Humphreys, A.P. Sutton, Electron-energy-loss spectra and the structural stability of nickel oxide: an LSDA+U study, Phys. Rev. B 57 (1998) 1505–1509, http://dx.doi.org/10.1103/PhysRevB.57.1505.

[44] A.K. Mishra, A. Roldan, N.H. de Leeuw, CuO surfaces and CO_2 activation: a dispersion-corrected DFT+ U study, J. Phys. Chem. C. 120 (2016) 2198–2214, http://dx.doi.org/10.1021/acs.jpcc.5b10431.

[45] A.K. Mishra, A. Roldan, N.H. de Leeuw, A density functional theory study of the adsorption behaviour of CO_2 on Cu_2O surfaces, J. Chem. Phys. 145 (2016), 044709, http://dx.doi.org/10.1063/1.4958804.

[46] H.J. Monkhorst, J.D. Pack, Special points for Brillouin-zone integrations, Phys. Rev. B 13 (1976) 5188–5192, http://dx.doi.org/10.1103/PhysRevB.13.5188.

[47] S. Grimme, Semiempirical GGA-type density functional constructed with a long-range dispersion correction, J. Comput. Chem. 27 (2006) 1787–1799, http://dx.doi.org/10.1002/jcc.20495.

[48] G. Henkelman, A. Arnaldsson, H. Jónsson, A fast and robust algorithm for Bader decomposition of charge density, Comput. Mater. Sci. 36 (2006) 354–360, http://dx.doi.org/10.1016/j.commatsci.2005.04.010.

[49] R.F.W. Bader, Atoms in Molecules: a Quantum Theory, Oxford University Press, London, 1994 https://global.oup.com/academic/product/atoms-in-molecules-9780198558651#.XsEQe5nJ4Lg.mendeley.

[50] E. Ghanti, R. Nagarajan, Synthesis of $CuAl_2(acac)_4(O^iPr)_4$, its hydrolysis and formation of bulk $CuAl_2O_4$ from the hydrolyzed gels; a case study of molecules to materials, Dalton Trans. 39 (2010) 6056, http://dx.doi.org/10.1039/b926579a.

[51] N. Tomar, E. Ghanti, A.K. Bhagi, R. Nagarajan, Studies on the hydrolysis of $\{Cu[Al(OPr^i)_4]_2\}$, a single source precursor for $CuAl_2O_4$ spinel, J. Non. Solids 355 (2009) 2657–2662, http://dx.doi.org/10.1016/j.jnoncrysol.2009.08.026.

[52] M. Salavati-Niasari, F. Davar, M. Farhadi, Synthesis and characterization of spinel-type $CuAl_2O_4$ nanocrystalline by modified sol–gel method, J. Solgel Sci. Technol. 51 (2009) 48–52, http://dx.doi.org/10.1007/s10971-009-1940-3.

[53] S. Åsbrink, L.J. Norrby, A refinement of the crystal structure of copper(II) oxide with a discussion of some exceptional e.s.d.'s, Acta Crystallogr. Sect. B Struct. Crystallogr. Cryst. Chem. 26 (1970) 8–15, http://dx.doi.org/10.1107/S0567740870001838.

[54] I.M. Tiginyanu, O. Lupan, V.V. Ursaki, L. Chow, M. Enachi, Nanostructures of metal oxides, in: P. Bhattacharya, R. Fornari, H. Kamimura (Eds.), Compr. Semicond. Sci. Technol., Elsevier, Amsterdam, 2011, pp. 396–479, http://dx.doi.org/10.1016/B978-0-44-453153-7.00105-X.

[55] L. Debbichi, M.C. Marco de Lucas, J.F. Pierson, P. Krüger, Vibrational properties of CuO and Cu_4O_3 from first-principles calculations, and Raman and infrared spectroscopy, J. Phys. Chem. C. 116 (2012) 10232–10237, http://dx.doi.org/10.1021/jp303096m.

[56] D. Wu, Q. Zhang, M. Tao, LSDA+U study of cupric oxide: electronic structure and native point defects, Phys. Rev. B 73 (2006) 235206–235212, http://dx.doi.org/10.1103/PhysRevB.73.235206.

[57] J.D. Hanawalt, H.W. Rinn, L.K. Frevel, Chemical analysis by X-Ray diffraction, Ind. Eng. Chem. Anal. Ed. 10 (1938) 457–512, http://dx.doi.org/10.1021/ac50125a001.

[58] G. Kliche, Z.V. Popovic, Far-infrared spectroscopic investigations on CuO, Phys. Rev. B 42 (1990) 10060–10066, http://dx.doi.org/10.1103/PhysRevB.42.10060.

[59] H. Shirai, Y. Morioka, I. Nakagawa, Infrared and Raman Spectra and lattice vibrations of some oxide spinels, J. Phys. Soc. Japan. 51 (1982) 592–597, http://dx.doi.org/10.1143/JPSJ.51.592.

[60] M.A. Laguna-Bercero, M.L. Sanjuán, R.I. Merino, Raman spectroscopic study of cation disorder in poly- and single crystals of the nickel aluminate spinel, J. Phys. Condens. Matter 19 (2007) 186217, http://dx.doi.org/10.1088/0953-8984/19/18/186217.

[61] N. Ababii, M. Hoppe, S. Shree, A. Vahl, M. Ulfa, T. Pauporté, B. Viana, V. Cretu, N. Magariu, V. Postica, V. Sontea, M.-I. Terasa, O. Polonskyi, F. Faupel, R. Adelung, O. Lupan, Effect of noble metal functionalization and film thickness on sensing properties of sprayed TiO_2 ultra-thin films, Sensors Actuators A Phys. 293 (2019) 242–258, http://dx.doi.org/10.1016/j.sna.2019.04.017.

[62] F. Guanghui, D. Jiafeng, P. Donghui, H. Ouli, The migration of alkali ions from glass substrates coated with sol-gel barrier films, J. Non. Solids 112 (1989) 454–457, http://dx.doi.org/10.1016/0022-3093(89)90572-3.

[63] A. Loubat, M. Bouttemy, S. Gaiaschi, D. Aureau, M. Frégnaux, D. Mercier, J. Vigneron, P. Chapon, A. Etcheberry, Chemical engineering of Cu(in,Ga)Se_2 surfaces: an absolute deoxidation studied by X-ray photoelectron

spectroscopy and Auger electron spectroscopy signatures, Thin Solid Films 633 (2017) 87–91, http://dx.doi.org/10.1016/j.tsf.2016.10.013.

[64] A.V. Naumkin, A. Kraust-Vass, S.W. Gaarenstroom, C.J. Powell, NIST X-ray Photoelectron Spectroscopy Database, National Institute of Standards and Technology, 2000, http://dx.doi.org/10.18434/T4T88K, NIST Stand. Ref. Database Number 20.

[65] N. Pauly, S. Tougaard, F. Yubero, Determination of the Cu 2p primary excitation spectra for Cu, Cu$_2$O and CuO, Surf. Sci. 620 (2014) 17–22, http://dx.doi.org/10.1016/j.susc.2013.10.009.

[66] A. Vahl, J. Dittmann, J. Jetter, S. Veziroglu, S. Shree, N. Ababii, O. Lupan, O.C. Aktas, T. Strunskus, E. Quandt, R. Adelung, S.K. Sharma, F. Faupel, The impact of O$_2$/Ar ratio on morphology and functional properties of reactive sputtering of metal oxide thin films, Nanotechnology. 30 (2019), 235603, http://dx.doi.org/10.1088/1361-6528/ab0837.

[67] A.W. Golubkov, D. Fuchs, J. Wagner, H. Wiltsche, C. Stangl, G. Fauler, G. Voitic, A. Thaler, V. Hacker, Thermal-runaway experiments on consumer Li-ion batteries with metal-oxide and olivin-type cathodes, RSC Adv. 4 (2014) 3633–3642, http://dx.doi.org/10.1039/c3ra45748f.

[68] M. Metzger, B. Strehle, S. Solchenbach, H.A. Gasteiger, Origin of H$_2$ Evolution in LIBs: H$_2$O Reduction vs. Electrolyte Oxidation, J. Electrochem. Soc. 163 (2016) A798–A809, http://dx.doi.org/10.1149/2.1151605jes.

[69] D. Ortiz, V. Steinmetz, D. Durand, S. Legand, V. Dauvois, P. Maître, S. Le Caër, Radiolysis as a solution for accelerated ageing studies of electrolytes in Lithium-ion batteries, Nat. Commun. 6 (2015) 6950, http://dx.doi.org/10.1038/ncomms7950.

[70] N.E. Galushkin, N.N. Yazvinskaya, D.N. Galushkin, Mechanism of gases generation during lithium-ion batteries cycling, J. Electrochem. Soc. 166 (2019) A897–A908, http://dx.doi.org/10.1149/2.0041906jes.

[71] V. Mateev, I. Marinova, Z. Kartunov, Gas leakage source detection for Li-Ion batteries by distributed sensor array, Sensors. 19 (2019) 2900, http://dx.doi.org/10.3390/s19132900.

[72] M. Wenger, R. Waller, V.R.H. Lorentz, M. Marz, M. Herold, Investigation of gas sensing in large lithium-ion battery systems for early fault detection and safety improvement, in: IECON 2014 - 40th Annu. Conf. IEEE Ind. Electron. Soc., IEEE, 2014, pp. 5654–5659, http://dx.doi.org/10.1109/IECON.2014.7049366.

[73] O. Lupan, V. Postica, J. Gröttrup, A.K. Mishra, N.H. de Leeuw, J.F.C. Carreira, J. Rodrigues, N. Ben Sedrine, M.R. Correia, T. Monteiro, V. Cretu, I. Tiginyanu, D. Smazna, Y.K. Mishra, R. Adelung, Hybridization of zinc oxide tetrapods for selective gas sensing applications, ACS Appl. Mater. Interfaces 9 (2017) 4084–4099, http://dx.doi.org/10.1021/acsami.6b11337.

[74] L. Siebert, N. Wolff, N. Ababii, M.-I. Terasa, O. Lupan, A. Vahl, V. Duppel, H. Qiu, M. Tienken, M. Mirabelli, V. Sontea, F. Faupel, L. Kienle, R. Adelung, Facile fabrication of semiconducting oxide nanostructures by direct ink writing of readily available metal microparticles and their application as low power acetone gas sensors, Nano Energy 70 (2020), 104420, http://dx.doi.org/10.1016/j.nanoen.2019.104420.

[75] L. Siebert, O. Lupan, M. Mirabelli, N. Ababii, M.-I. Terasa, S. Kaps, V. Cretu, A. Vahl, F. Faupel, R. Adelung, 3D-printed chemiresistive sensor array on nanowire CuO/Cu$_2$O/Cu heterojunction nets, ACS Appl. Mater. Interfaces 11 (2019) 25508–25515, http://dx.doi.org/10.1021/acsami.9b04385.

[76] M. Hoppe, N. Ababii, V. Postica, O. Lupan, O. Polonskyi, F. Schütt, S. Kaps, L.F. Sukhodub, V. Sontea, T. Strunskus, F. Faupel, R. Adelung, (CuO-Cu$_2$O)/ZnO:Al heterojunctions for volatile organic compound detection, Sens. Actuators B Chem. 255 (2018) 1362–1375, http://dx.doi.org/10.1016/j.snb.2017.08.135.

[77] J. Gröttrup, V. Postica, N. Ababii, O. Lupan, C. Zamponi, D. Meyners, Y.K. Mishra, V. Sontea, I. Tiginyanu, R. Adelung, Size-dependent UV and gas sensing response of individual Fe$_2$O$_3$-ZnO:Fe micro- and nanowire based devices, J. Alloys. Compd. 701 (2017) 920–925, http://dx.doi.org/10.1016/j.jallcom.2016.12.346.

[78] N. Barsan, U. Weimar, Conduction model of metal oxide gas sensors, J. Electroceramics. 7 (2001) 143–167, http://dx.doi.org/10.1023/A:1014405811371.

[79] Y. Wang, K. Wu, As a whole: crystalline zinc aluminate nanotube array−Nanonet, J. Am. Chem. Soc. 127 (2005) 9686–9687, http://dx.doi.org/10.1021/ja0505402.

[80] M. Hoppe, O. Lupan, V. Postica, N. Wolff, V. Duppel, L. Kienle, I. Tiginyanu, R. Adelung, ZnAl$_2$O$_4$-Functionalized zinc oxide microstructures for highly selective hydrogen gas sensing applications, Phys. Status Solidi 215 (2018) 1700772, http://dx.doi.org/10.1002/pssa.201700772.

[81] C.R. Michel, CO and CO$_2$ gas sensing properties of mesoporous CoAl$_2$O$_4$, Sens. Actuators B Chem. 147 (2010) 635–641, http://dx.doi.org/10.1016/j.snb.2010.04.013.

[82] D. Dhak, P. Pramanik, Particle size comparison of soft-chemically prepared transition metal (Co, Ni, Cu, Zn) aluminate spinels, J. Am. Ceram. Soc. 89 (2006) 1014–1021, http://dx.doi.org/10.1111/j.1551-2916.2005.00769.x.

[83] O. Lupan, V. Cretu, V. Postica, O. Polonskyi, N. Ababii, F. Schütt, V. Kaidas, F. Faupel, R. Adelung, Non-planar nanoscale p–p heterojunctions formation in Zn$_x$Cu$_{1-x}$O$_y$ nanocrystals by mixed phases for enhanced sensors, Sens. Actuators B Chem. 230 (2016) 832–843, http://dx.doi.org/10.1016/j.snb.2016.02.089.

[84] X. Zhao, L. Wang, X. Xu, X. Lei, S. Xu, F. Zhang, Fabrication and photocatalytic properties of novel ZnO/ZnAl$_2$O$_4$ nanocomposite with ZnAl$_2$O$_4$ dispersed inside ZnO network, AIChE J. 58 (2012) 573–582, http://dx.doi.org/10.1002/aic.12597.

[85] H.-J. Kim, H.-M. Jeong, T.-H. Kim, J.-H. Chung, Y.C. Kang, J.-H. Lee, Enhanced ethanol sensing characteristics of In$_2$O$_3$ -Decorated NiO hollow nanostructures via modulation of hole accumulation layers, ACS Appl. Mater. Interfaces 6 (2014) 18197–18204, http://dx.doi.org/10.1021/am5051923.

[86] H.-R. Kim, K.-I. Choi, K.-M. Kim, I.-D. Kim, G. Cao, J.-H. Lee, Ultra-fast responding and recovering C$_2$H$_5$OH sensors using SnO$_2$ hollow spheres prepared and activated by Ni templates, Chem. Commun. 46 (2010) 5061, http://dx.doi.org/10.1039/c0cc00213e.

[87] O. Lupan, L. Chow, G. Chai, A single ZnO tetrapod-based sensor, Sens. Actuators B Chem. 141 (2009) 511–517, http://dx.doi.org/10.1016/j.snb.2009.07.011.

[88] O. Lupan, L. Chow, T. Pauporté, L.K. Ono, B. Roldan Cuenya, G. Chai, Highly sensitive and selective hydrogen single-nanowire nanosensor, Sens. Actuators B Chem. 173 (2012) 772–780, http://dx.doi.org/10.1016/j.snb.2012.07.111.

[89] Y.-H. Choi, D.-H. Kim, S.-H. Hong, K.S. Hong, H$_2$ and C$_2$H$_5$OH sensing characteristics of mesoporous p-type CuO films prepared via a novel precursor-based ink solution route, Sens. Actuators B Chem. 178 (2013) 395–403, http://dx.doi.org/10.1016/j.snb.2012.12.096.

[90] M. Bersani, K. Gupta, A.K. Mishra, R. Lanza, S.F.R. Taylor, H.-U. Islam, N. Hollingsworth, C. Hardacre, N.H. de Leeuw, J.A. Darr, Combined EXAFS, XRD, DRIFTS, and DFT Study of Nano Copper-Based Catalysts for CO$_2$ Hydrogenation, ACS Catal. 6 (2016) 5823–5833, http://dx.doi.org/10.1021/acscatal.6b01529.

Biographies

Oleg Lupan is a fellow for experienced researchers supported by Alexander von Humboldt Foundation at *Kiel University, Christian-Albrechts Universität zu Kiel* (CAU) in research group "Functional Nanomaterials" of Professor Adelung, Germany. He received his M.S. in microelectronics and semiconductor devices from the Technical University of Moldova (TUM) in 1993. He received his Ph.D. from the Institute of Applied Physics, Academy of Sciences of Moldova (ASM) in 2005. His post-doctorate research activities were carried out at the French CNRS, Paris, France and the University of Central Florida, USA. He received his doctor habilitate degree (Dr. Eng.) in solid state electronics, microelectronics and nanoelectronics from the Institute of Electronic Engineering and Nanotechnologies of ASM in 2011 and his Thesis was ranked as number one in 2011 year by the CNAA. His post-habilitation activities were performed at the University of Paris-PSL-IRCP-ENSCP-CNRS, Paris, France and the Institute for Materials Science, University of Kiel CAU, Germany. He is a Professor and senior research scientist in solid state electronics and nanoelectronics at TUM. He started a new research group "Nanotechnology and Nanosensors" in 2015. Lupan holds professorial appointments at the University of Central Florida, USA. His current research interests include nanotechnologies and nanomaterials for sensors, optoelectronic devices, and other nanodevices. H-index is 54, Scopus. E-mail: ollu@tf.uni-kiel.de, oleg.lupan@mib.utm.md More details are given at https://utm.md/

Ababii Nicolai is at present a Ph. D. candidate in the group of Nanotechnologies for sensing nanodevices, TUM, Moldova. He worked in the field of copper oxide nanocomposite and its surface control for his Engineering degree diploma and continued for master thesis in Nanotechnologies at Technical University of Moldova. He received his M.Sc. in microelectronics and nanotechnologies from the Technical University of Moldova in 2016. His current research interests are nanostructuring of semiconducting oxide thin films and nanowires for gas sensors. More details are given at http://mib.utm.md/

Abhishek Kumar Mishra is a computational material scientist having over 50 publications in materials modelling and simulation field. Dr. Mishra research interest is in electronic structure calculations employing first-principles based simulations. He is working as Associate Professor at University of Petroleum and Energy Studies (UPES), Dehradun, India. He completed Ph.D. in Computational Physics from University of Lucknow in 2009 and worked for more than eight years as postdoctoral researcher before joining UPES, Dehradun in 2016. His first post-doctoral position was at Texas A&M University, TX, USA (2010), which was followed by DST Fast Track Fellow position at JNCASR, Bangalore (2010–2013) and EPSRC PDRA position at University College London, London (2013–2016). His present research interest includes investigating materials for CO$_2$ capture and conversion, gas sensors, 2d materials hetrostructures, materials for batteries and nano-electronics. He also worked as post-doctorate research associate at Banaras Hindu University, Varanasi and Guest Scientist at ICTP, Italy (2012).

Mani Teja Bodduluri is currently working as a PhD student at the chair of Materials and Processes for Nanosystem Technologies at the Institute for Materials Science, Faculty of Engineering, Kiel University, Germany.

Nicolae Magariu is a Ph. D. candidate in the group of Nanotechnology and Nanosensors of Prof. Lupan, TUM, Moldova. He worked in the field of zinc oxide-copper oxide composite and its surface modification for his Engineering degree diploma and continued for master thesis in Nanotechnologies at TUM. He received his M.Sc. in microelectronics and nanotechnologies from the TUM in 2017. His current research interests are nanostructuring of semiconducting oxides, thin films and nanowires, gas sensors, nanosensors and UV photodetectors' development. More details are given at http://mib.utm.md/

Alexander Vahl studied Materials Science at Kiel University (2009–2014). He wrote his dissertation at the Chair of Prof. F. Faupel (Multicomponent Materials) on the topic of memristive switching and memsensor devices and obtained his Ph.D. from the Faculty of Engineering in 2019. Since 2019 he is working as postdoc in the group "Multicomponent Materials" of Prof. F. Faupel at Faculty of Engineering at Kiel University. His field of study includes memristive, memsensitive and sensor thin film devices with a special focus on nanoparticle composites.

Helge Krüger is currently working as a PhD student at the chair of Functional Nano-materials (Prof. Dr. Rainer Adelung) at the Institute for Materials Science, Faculty of Engineering, Kiel University, Germany.

Bernhard Wagner is full professor and chair holder of the Materials and Processes for Nanosystem Technologies at the Institute for Materials Science, Kiel University, Germany.

Rainer Adelung is full professor and chair holder of the Functional Nanomaterials group established in 2007 at the Institute for Materials Science, Kiel University, Germany. He received his Ph.D. (rer. nat.) in physics in 2000 from the Institute of Experimental and Applied Physics, Kiel University, and during 2001–2002 he was at Case Western Reserve University in Cleveland (USA) as Feodor Lynen (Alexander von Humboldt) research fellow. In 2006 he finished his habilitation at the Institute for Materials Science in Kiel and then continued as Heisenberg Professor (DFG grant) with his own Functional Nanomaterials group in 2012. More information at https://www.tf.uni-kiel.de/matwis/fnano/de.

Franz Faupel received his Ph.D. in physics from the University of Göttingen in 1985. He was postdoctoral fellow at the IBM Research Center Yorktown Heights and got his habilitation in 1992. Since 1994, he holds the Chair for Multicomponent Materials at Kiel University. Prof. Faupel is Chairman of the North German Initiative Nanotechnology and has served on various editorial boards including Journal of Materials Research, SN Applied Sciences, Materials, Applied Physics Letters, and Journal of Applied Physics. He published more than 375 papers, and his Web of Sciences h index is 50. His research interests include functional nanocomposites, magnetoelectric sensors, photocatalysis, and plasma deposition. More details are given at www.tf.uni-kiel.de/matwis/matv.

Nora H. de Leeuw is a prominent scientist with an international reputation in the field of computational chemistry of materials and minerals. Specific research interests include materials for sustainable energy applications, the development of models to study biocompatible materials for tissue engineering applications, and the computer-aided design of sustainable catalysts for the conversion of carbon dioxide to fuels and chemicals under mild reaction conditions. De Leeuw holds professorial appointments at the University of Leeds, UK, and Utrecht University, the Netherlands, and she has been awarded research fellowships by the EPSRC and Royal Society and a William Penney fellowship by AWE. She is the recipient of a Royal Society Wolfson Merit Award, elected Fellow of the Learned Society of Wales, and Member of Academia Europaea.

Sandra Hansen is Post-Doc and Habilitation Candidate at the chair for Functional Nanomaterials at the Department of Engineering of the Christian-Albrechts-University Kiel, Germany. She received her Ph.D. in November 2017 in Materials Science, Kiel University, as best dissertation of this year. During her stay at SLAC, Stanford University, CA, USA, she learned fundamental structural knowledge of full silicon anodes for Lithium-Ion Batteries. Since 2017 she is leading an independent research group of battery technology and development at the chair of Functional Nanomaterials. Her research focuses on the synthesis, fabrication and characterization of novel and innovative battery materials for Li-ion batteries, but also for the post-Li generation, memristive devices, battery electrolytes.